Probabilistic Engineering Mechanics
To: Prof. P.D. Spanos, Editor
--Manuscript Draft--

Manuscript Number:	
Article Type:	Full Length Article
Keywords:	state formulation, complex eigenproblem, multiiple timescale spectral analysis, resonant component, loading component, background, inertial
Corresponding Author:	Margaux Geuzaine University of Liège Liège, BELGIUM
First Author:	Margaux Geuzaine
Order of Authors:	Margaux Geuzaine
	Aksel Fenerci
	Ole Andre Øiseth
	Vincent Denoël
Abstract:	Abstract The determination of the long-term extreme distribution for a wave-loaded structure requires to compute the second order statistics of the responses and their time derivatives under various short-term sea states. In a spectral context, these statistics are typically obtained in the modal basis by integrating the cross-spectral densities of the corresponding responses over the frequency. In this paper, a semi-analytical approximation is developed for computing these integrals, in order to reduce the computational cost of each short-term analysis. To do so, a state-space formulation is considered for the equations of motion and the general framework provided by the multiple timescale spectral analysis is implemented. It hinges on the existence of distinct peaks in the integrands to express the variances and the covariances of the modal state responses as the sum of two components with simple expressions: the resonant and the loading component. The proposed approximation is validated on a minimalistic example first and is then verified on a simplified model inspired by the Bergsøysund Bridge, an actual floating pontoon bridge.
Suggested Reviewers:	George Deodatis deodatis@columbia.edu
	Francesco Foti francesco.foti@polimi.it
	Knut Andreas Kvale knut.a.kvale@ntnu.no
	Antonina Pirotta antonina.pirrotta@unipa.it
	Ioannis Kougioumtzoglou ikougioum@columbia.edu
Opposed Reviewers:	

To: Prof. P.D. Spanos, Editor

Liège, January 19th, 2022.

Re: Paper submission to Probabilistic Engineering Mechanics

Dear Prof. Spanos,

Please consider this submission as an interesting potential paper for the Probabilistic Engineering Mechanics.

As you will readily discover, it concerns the extension of the multiple timescale spectral analysis to wave-loaded structures. The original formulation of this method has actually been presented in your journal. It has then been applied to a linear fractional viscoelastic system in another of your publications. We therefore do believe it is the best medium to disseminate the results of this work.

For the moment, the multiple timescale spectral analysis has mainly been applied to wind-loaded structures which are typically excited in their quasi-static and resonant regimes. The first novelty in this paper is related to the fact that wave-loaded structures are expected to respond in the inertial regime as well. The second novelty consists in adopting a state formulation for the equations of motion, meaning that the associated eigenproblem is complex. The background and the resonant components, which are well known in wind engineering, are therefore revisited and generalized in this broader context.

We do very humbly and honestly believe this manuscript would be a fair contribution to the advancement of knowledge in the field of Probabilistic Mechanics. While hoping this submission will be received with enthusiastic and helpful reviews, of course with the examination level corresponding to your standards, on behalf of the authors, I wish to warmly acknowledge the attention You, the Edition team and Referees will pay to this submission.

Kind regards,

Geuzaine M

Ir. Margaux Geuzaine
University of Liège

Multiple timescale spectral analysis of floating structures subjected to hydrodynamic loads

Margaux Geuzaine[a,b], Aksel Fenerci[c], Ole Øiseth[d], Vincent Denoël[a]

[a] *Structural & Stochastic Dynamics, UEE Department, University of Liège,*
[b] *F.R.S.-FNRS, Belgian Fund for Scientific Research*
[c] *Department of Ocean Operations and Civil Enginering, Norwegian University of Science and Technology*
[d] *Department of Structural Engineering, Norwegian University of Science and Technology*

Abstract

The determination of the long-term extreme distribution for a wave-loaded structure requires to compute the second order statistics of the responses and their time derivatives under various short-term sea states. In a spectral context, these statistics are typically obtained in the modal basis by integrating the cross-spectral densities of the corresponding responses over the frequency. In this paper, a semi-analytical approximation is developed for computing these integrals, in order to reduce the computational cost of each short-term analysis. To do so, a state-space formulation is considered for the equations of motion and the general framework provided by the multiple timescale spectral analysis is implemented. It hinges on the existence of distinct peaks in the integrands to express the variances and the covariances of the modal state responses as the sum of two components with simple expressions: the resonant and the loading component. The proposed approximation is validated on a minimalistic example first and is then verified on a simplified model inspired by the Bergsøysund Bridge, an actual floating pontoon bridge.

Keywords: state formulation, complex eigenproblem, multiiple timescale spectral analysis, resonant component, loading component, background, inertial

Highlights:

- The multiple timescale spectral analysis is applied to wave-loaded structures.
- Semi-analytical approximations are provided for the modal state covariances.
- They are decomposed into a resonant and a loading component (background/inertial).
- Resorting to this approach drastically reduces the computational demand.

1. Introduction

In the past several decades, the design of very large floating structures has attracted considerable attention because they offer viable solutions to respond to many of our needs and problems [41, 14]. For instance, the crossing of wide and deep straits, as in Norway [32] and China [31], could not be completed without having recourse to floating bridges or tunnels [44, 8]. Floating facilities are also able to provide extensions for coastal areas where land reclamations are not economically or environmentally reasonable while floating solar platforms and energy hubs are expected to support the energy transition.

As long as no significant nonlinearities related to mooring effects or extreme conditions are considered —for example when an end-anchored floating bridge with discretely distributed pontoons such as the Bergsøysund Bridge in Norway is subjected to ordinary waves— the hydrodynamic analysis of very large floating structures can be performed more efficiently in the frequency domain than in the time domain [42, 43]. Indeed, it is no longer necessary to measure nor to simulate long time histories with short time steps in order to capture both the slow and the fast dynamics of the responses. In a spectral approach, the loading and the structure are defined in the frequency domain by means of power spectral densities and frequency response functions whose combined products give the power spectral densities of structural responses [29, 12].

The variances of the response processes and their time derivatives are useful for determining the short-term extreme distribution [33] and accumulated damage [37]. They can be obtained by integrating the corresponding power spectral densities over frequency. But, even though the analysis is performed in the frequency domain using modal truncation techniques, this remains a computationally demanding operation because of two main issues. First, heavy computations have to be repeated at each integration point, as for instance the establishment of the matrix containing the cross-spectral densities of the loadings applied on the numerous structural degrees-of-freedom, or the projection of such large matrices into the modal basis. Second, computing the integral with a sufficient accuracy requires to use many closely spaced points, spread over a wide domain because the integrands typically feature several sharp and distant peaks related to the resonance of the structure in its multiple modes and to the particular energy content of the wave loads. Moreover, these short-term analyses have to be executed for many different sea states before being concatenated and weighted by their probability of occurence in order to provide long-term evaluations for the extreme distributions [3] and fatigue accumulations [34], which are necessary to ensure that the structure is designed properly and is expected to stay safe over its whole lifetime with a sufficiently high probability given the possible variation of the sea states in time [33].

Over the years, many studies have explored the possibility to reduce this computational burden for various marine structures, such as floating offshore wind turbines [4] or floating bridges [18], by focusing on the long-term analysis and by using for instance the first and second order reliability methods, the inverse reliability method, or the environmental contour approach but also surrogate modelling or learning algorithms [17, 21, 45, 30, 22]. Apart from that, another way for improving the computational efficiency of the long-term analyses is to accelerate each of the many short-term analyses that have to be conducted. To do so, Giske et al. have recently proposed to estimate the cross-spectral densities of the loadings by using Fourier series [20]. But, although they are obtained much more rapidly than before, they still have to be projected into the modal basis for a lot of frequencies. This latter problem is thus tackled in the following paper by deriving semi-analytical approximations for the integrals at stake, which allow to drastically reduce the number of times such a time consuming operation is achieved.

Davenport was the first to formulate such an approximate solution for the variances of the modal responses of a structure under buffeting wind loads [7]. Then, Gu [23] and Denoël [9] independently did the same for the covariances of the modal responses in a wind engineering context as well, in order to get the variances of the nodal responses in an efficient way through a complete quadratic combination scheme. At this point, however, some assumptions such as the replacement of the power and cross-spectral densities by a constant (white-noise) were not fully justified, mathematically speaking [10]. This was done later on when Denoël hinged on the existence of well separated timescales in the buffeting responses to develop the multiple timescale spectral analysis [12]. This general framework is based on the perturbation theory and aims at expressing simple expressions to approximate the statistics of the responses very quickly with a controllable discrepancy [25].

For the moment, though, it has mainly been used to deal with slightly damped wind-loaded structures which are typically excited in their quasi-static and resonant regimes, meaning that the statistics can be decomposed into a background and a resonant component [24, 11, 13]. The multiple timescale spectral analysis is specialized in this paper to the second order statistics of the responses of wave-loaded structures, with the major and new specificity that they might respond in the inertial regime as well. A dedicated approximation is therefore derived to capture this type of behavior. A second novelty presented in this paper consists in adopting a state formulation for the equations of motion as it allows to decouple the modal responses even though the hydrodynamic damping is considered [16, 26, 1]. Overall, new expressions are thus established in this paper, not only for the inertial component, but also for the background and the resonant components of the modal state covariances. To start, governing equations are presented in Section 3. Then, the multiple timescale spectral analysis is introduced, applied to the problem at hand and the resulting formulas are verified on a minimalistic example in Section 4. Illustrations are finally provided in Section 5 for a simplified 2D model inspired by the Bergsøysund Bridge.

2. Nomenclature - Notations

Lowercase and capital bold letters are respectively used for denoting vectors and matrices while italic letters are employed for their elements. The superscripts $(.)^*$, $(.)^\intercal$ and $(.)^\dagger$ stand for the conjugate, the transpose and the conjugate transpose (hermitian) operators.

3. Problem Statement

3.1. State Space Formulation

The dynamics of a linear elastic structure with N degrees-of-freedom subjected to sea waves is governed by a set of N second order differential equations whose Fourier transform reads

$$\left[\mathbf{K}_\mathrm{s} + \mathrm{i}\omega\mathbf{C}_\mathrm{s} - \omega^2\mathbf{M}_\mathrm{s}\right]\mathbf{x}\left(\omega\right) = \mathbf{f}_\mathrm{h}\left(\omega\right) \tag{1}$$

where i is the imaginary unit, ω is the circular frequency, $\mathbf{x}\left(\omega\right)$ and $\mathbf{f}_\mathrm{h}\left(\omega\right)$ are two $N \times 1$ vectors containing the frequency-domain representations of the structural displacements in every degree-of-freedom and the total hydrodynamic loads acting on each of them, respectively, while $\mathbf{K}_\mathrm{s}$, $\mathbf{C}_\mathrm{s}$, and $\mathbf{M}_\mathrm{s}$ denote the $N \times N$ structural stiffness, damping and mass matrices which are typically real and symmetric within a finite element modelling framework [46, 2].

Besides the total hydrodynamic actions are generally expressed in the frequency domain by

$$\mathbf{f}_\mathrm{h}\left(\omega\right) = \mathbf{f}\left(\omega\right) - \left[\mathbf{K}_\mathrm{h}\left(\omega\right) + \mathrm{i}\omega\mathbf{C}_\mathrm{h}\left(\omega\right) - \omega^2\mathbf{M}_\mathrm{h}\left(\omega\right)\right]\mathbf{x}\left(\omega\right) \tag{2}$$

where the first term is due to the undisturbed waves and the other ones are originating from the interactions between the relative motion of the fluid and the structure which gives rise to additional elastic, viscous and inertial forces, as indicated by the hydrodynamic stiffness, damping and mass matrices, $\mathbf{K}_\mathrm{h}\left(\omega\right)$, $\mathbf{C}_\mathrm{h}\left(\omega\right)$, and $\mathbf{M}_\mathrm{h}\left(\omega\right)$. In numerical studies, their determination frequently relies on the potential theory, which is fundamentally linear and thus allows to superimpose the well-known flow fields obtained with the panel method when the body is supposed to oscillate in still water or when it is fixed and exposed to sinuisoidal waves of unit height, by assuming that the steepness of the waves is small, the fluid motion is irrotational and the water is inviscid and incompressible [15].

The supplemental stiffness matrix is usually independent of the frequency whereas the added damping and mass matrices are not. As a first approximation, though, they can be evaluated at the dominant frequency of the forces or of the motions, which is denoted ω_0 here, and hence be considered as constant as well provided their frequency sensitivity is limited [41, 28, 39]. Under these conditions, Equation (1) becomes

$$\left[\mathbf{K} + \mathrm{i}\omega\mathbf{C} - \omega^2\mathbf{M}\right]\mathbf{x}(\omega) = \mathbf{f}(\omega) \tag{3}$$

where the global hydroelastic matrices read $\mathbf{K} = \mathbf{K}_\mathrm{s} + \mathbf{K}_\mathrm{h}(\omega_0)$, $\mathbf{C} = \mathbf{C}_\mathrm{s} + \mathbf{C}_\mathrm{h}(\omega_0)$, and $\mathbf{M} = \mathbf{M}_\mathrm{s} + \mathbf{M}_\mathrm{h}(\omega_0)$.

The state variables $\mathbf{y}(\omega) = \begin{bmatrix} \mathbf{I} & \mathrm{i}\omega\mathbf{I} \end{bmatrix}^\intercal \mathbf{x}(\omega)$ and the state forces $\mathbf{g}(\omega) = \begin{bmatrix} \mathbf{I} & \mathbf{0} \end{bmatrix}^\intercal \mathbf{f}(\omega)$, with $\mathbf{I}$ and $\mathbf{0}$ being respectively the $N \times N$ identity and zero matrices, can be introduced to recast the N second-order equations into $2N$ first-order equations as follows

$$[\mathbf{A} + \mathrm{i}\omega\mathbf{B}]\,\mathbf{y}(\omega) = \mathbf{g}(\omega) \tag{4}$$

where the state matrices are defined by

$$\mathbf{A} = \begin{bmatrix} \mathbf{K} & \mathbf{0} \\ \mathbf{0} & -\mathbf{M} \end{bmatrix} \quad \text{and} \quad \mathbf{B} = \begin{bmatrix} \mathbf{C} & \mathbf{M} \\ \mathbf{M} & \mathbf{0} \end{bmatrix}. \tag{5}$$

This form conserves the symmetry and postive definiteness of $\mathbf{K}$, $\mathbf{C}$ and $\mathbf{M}$ [40, 16, 35].

Although this formulation doubles the size of the problem, i.e. $[\mathbf{A} + \mathrm{i}\omega\mathbf{B}]$ versus $\left[\mathbf{K} + \mathrm{i}\omega\mathbf{C} - \omega^2\mathbf{M}\right]$, the state matrices actually have the advantage to be simultaneously diagonalizable even if the hydrodynamic damping is neither classical [26, 5], nor negligible [28, 36]. Resorting to such an approach is therefore necessary to find an appropriate projection space in which the modal state responses can be completely decoupled and can thus be obtained independently of one another, without requiring any costly matrix inversion.

3.2. Modal State Decomposition

To do so, the complex eigenproblem associated to the homogeneous part of the governing equations has first to be addressed. Although this operation can be numerically expensive as well, the eigensystem interestingly reads

$$\mathrm{i}\mathbf{A}\boldsymbol{\Theta} = \mathbf{B}\boldsymbol{\Theta}\boldsymbol{\Lambda} \tag{6}$$

and is thus linear in the eigenvalue matrix $\boldsymbol{\Lambda}$ instead of quadratic. It can consequently be solved with the help of very efficient algorithms in order to get the matrix of eigenfrequencies, $\boldsymbol{\Lambda} = \mathrm{diag}(\lambda_1, ..., \lambda_m, ..., \lambda_{2M})$, and the matrix of corresponding eigenmodes, $\boldsymbol{\Theta} = [\boldsymbol{\theta}_1, ..., \boldsymbol{\theta}_m, ..., \boldsymbol{\theta}_{2M}]$.

Moreover, keeping the first $2M \ll 2N$ contributing modes allows to considerably improve the computational efficiency without sacrificing accuracy. Indeed, higher modes of vibration are generally ignored because they tend to be less excited by the hydrodynamic loads and to be more affected by the discretization errors [36, 26].

By definition, the mode shapes coming from Equation (6) are orthogonal to each other with respect to both state matrices. Also they are normalized to yield

$$\mathbf{\Theta}^\intercal \mathbf{A} \mathbf{\Theta} = \mathbf{\Lambda} \mathbf{D}^{-1} \quad \text{and} \quad \mathbf{\Theta}^\intercal \mathbf{B} \mathbf{\Theta} = \mathrm{i} \mathbf{D}^{-1} \tag{7}$$

by selecting the elements of $\mathbf{D} = \mathrm{diag}\left(D_1, ..., D_m, ..., D_{2M}\right)$ in such a way that the real (resp. imaginary) part of the eigenvectors of odd rank (resp. even) reach a unit maximum absolute value. Besides, the eigenvalues are decomposed as such

$$\lambda_m = \psi_m + \mathrm{i}\upsilon_m \quad \text{with} \quad \psi_m = (-1)^m \sqrt{1 - \xi_{j_m}^2}\, \omega_{j_m} \quad \text{and} \quad \upsilon_m = \xi_{j_m}\, \omega_{j_m} \tag{8}$$

where ω_{j_m} and ξ_{j_m} are the j-th undamped natural frequency and critical damping ratio of the structure with $j_m = \left\lceil \frac{m}{2} \right\rceil$. These notation, normalization and organization choices eventually imply that the eigensolutions come in the following pairs $\lambda_m = -\lambda_{m+1}^*$ and $\boldsymbol{\theta}_m = -\mathrm{i}\boldsymbol{\theta}_{m+1}^*$ when m is odd.

The modal projection and decomposition of the state forces and responses, $\mathbf{p}(\omega) = \mathbf{\Theta}^\intercal \mathbf{g}(\omega)$ and $\mathbf{y}(\omega) = \mathbf{\Theta} \mathbf{q}(\omega)$, are then introduced into Equation (4) which is subsequently left-multiplied by $\Theta^\intercal$ and $\mathbf{DH}(\omega)$ to give

$$\mathbf{q}(\omega) = \mathbf{DH}(\omega)\, \mathbf{p}(\omega) \tag{9}$$

where $\mathbf{H}(\omega) = \mathrm{diag}\left(H_1(\omega), ..., H_m(\omega), ..., H_{2M}(\omega)\right)$ is the matrix of generalized frequency response functions. Being diagonal, this inverse matrix is not particularly expensive to calculate and Equation (9) can equivalently be written

$$q_m(\omega) = D_m H_m(\omega)\, p_m(\omega) \tag{10}$$

with $H_m(\omega) = (\lambda_m - \omega)^{-1}$. Each of these modal responses thus appears to be monochromatic, on top of being decoupled, because the corresponding frequency response function contains a single pole.

As a result, the real part of $H_m(\omega)$ exhibits a double peak, spiking just left and just right to $\omega = \psi_m$ with a sign change in between, while the imaginary part of $H_m(\omega)$ displays a single peak located at $\omega = \psi_m$. The position, the height and the width of these peaks are clearly shown on Figure 1-(a) which pictures the real and the imaginary parts of $H_m(\omega)$ in linear scales, with their signs, whereas Figure 1-(b) gives an overview of what happens far below and far above the peaks by presenting the real and the imaginary parts of $H_m(\omega)$ in absolute values and logarithmic scales. In particular, the slopes of the straight lines drawn at both extremities of this log-log plot indicate that $\Re\left[H_m(\omega)\right]$ and $\Im\left[H_m(\omega)\right]$ are approximately constant when $|\omega| \ll |\psi_m|$ and behave like monomials of degree (-1) or (-2), respectively, when $|\omega| \gg |\psi_m|$.

3.3. Spectral Analysis

Thanks to the introduction of the state variables and the modal coordinates, the responses of the structure can be determined in a very efficient way once forces are defined. In a stochastic analysis context, the probabilistic properties of the former processes can thus be derived in a similar fashion based on those of the latters, as detailed hereafter.

Since the static analysis of the structure is performed beforehand to define its reference configuration, the undisturbed wave loads have a zero mean. They can in addition be considered as Gaussian when dealing with deep

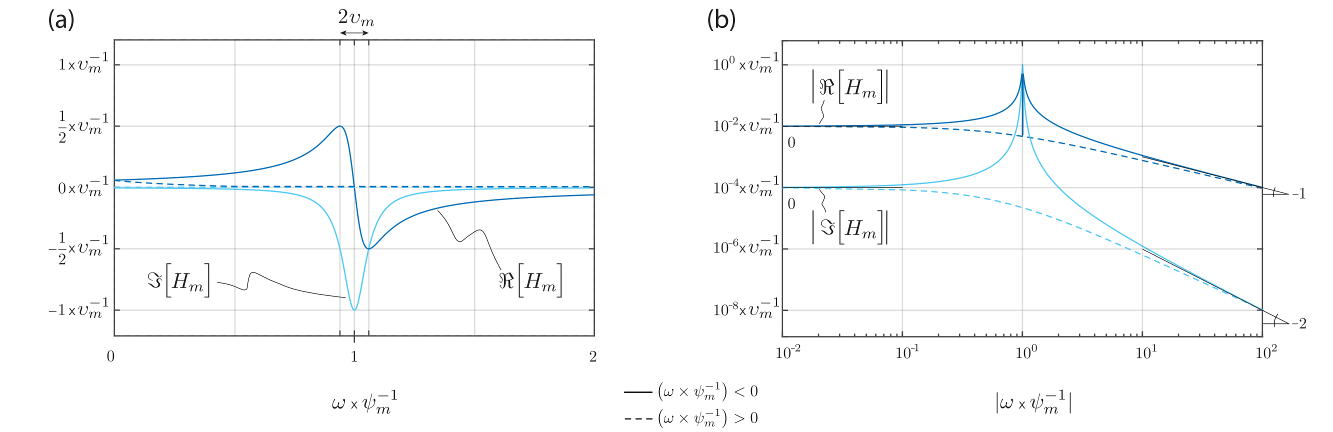

Figure 1: Real and imaginary parts of the m-th frequency response function: (a) with their sign in linear scales, (b) in absolute value and logarithmic scales.

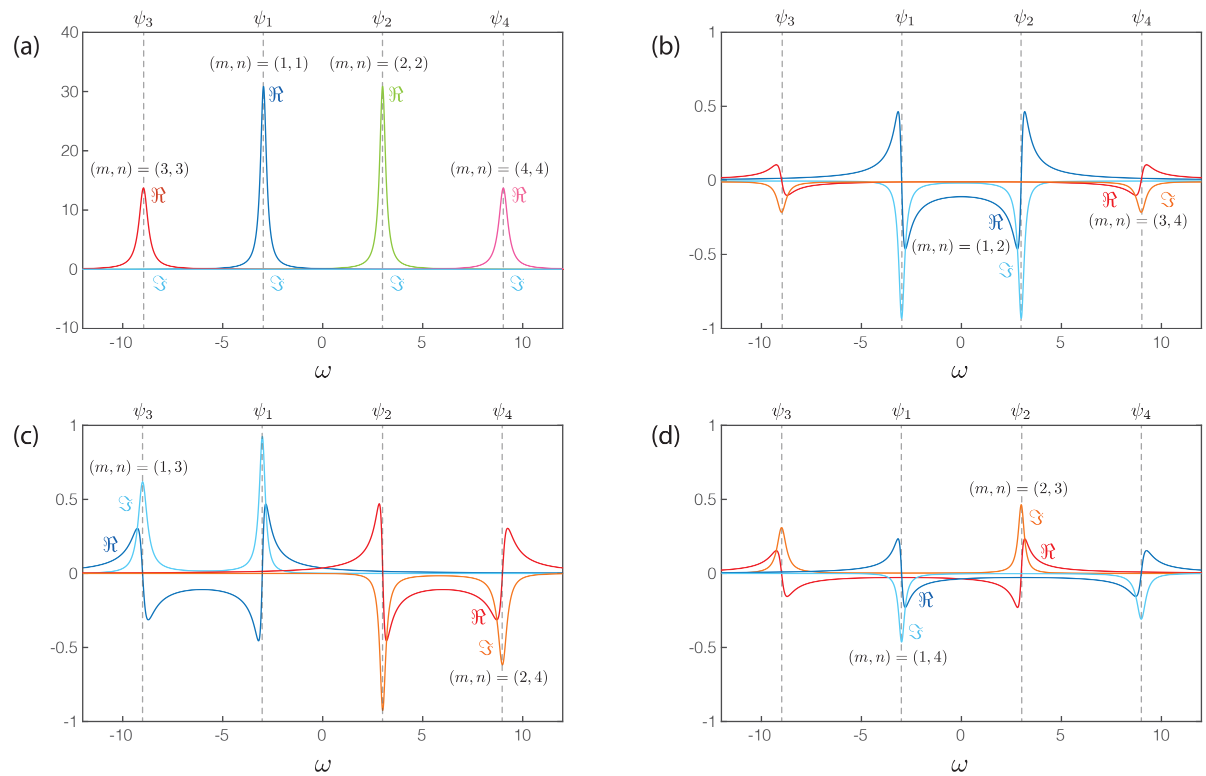

Figure 2: Real and imaginary parts of the structural kernel function when $\omega_1 = 3$ rad/s, $\omega_2 = 9$ rad/s, $\xi_1 = 0.06$, and $\xi_2 = 0.03$: (a) $|\psi_m| = |\psi_n|$ and $\psi_m \psi_n > 0$, (b) $|\psi_m| = |\psi_n|$ and $\psi_m \psi_n < 0$, (c) $|\psi_m| \neq |\psi_n|$ and $\psi_m \psi_n > 0$, (d) $|\psi_m| \neq |\psi_n|$ and $\psi_m \psi_n < 0$.

water waves of moderate heights [28]. In this event, their probabilistic behaviour is fully characterized on the sole basis of their cross-spectral densities, $S_{f,ij}(\omega)$. Establishing them is however not the purpose of the present paper, see e.g. [19] for that matter, but a few of their peculiarities are worthy to be highlighted for further discussion.

In brief, they are typically obtained by using a unidirectional wave spectrum whose unified expression reads

$$S_w(\omega) = \left(\frac{\omega_p^5}{\omega^5}\right) \exp\left(-\frac{5}{4}\frac{\omega_p^4}{\omega^4}\right) \tag{11}$$

and whose maximum is reached at ω_p in the positive frequency range [6]. Equation (11) is then commonly multiplied by other functions of the circular frequency, which include for instance the influence of directional spreading effects, spatial correlations, and wave elevation-to-force amplitude operators. Despite these modifications, the cross-spectral densities of the hydrodynamic forces ordinarily feature a similar exponential decay as $S_w(\omega)$ when the circular frequencies are approaching the origin while their energy content remains relatively clustered around ω_p which is hence referred to as the intrinsic frequency of the loading in the sequel [12].

After filling the matrix $\mathbf{S}_\mathrm{f}(\omega)$ with these cross-spectral densities, it can be used according to the definition of the state forces in the physical coordinates in order to build the matrix

$$\mathbf{S}_\mathrm{g}(\omega) = \begin{bmatrix} \mathbf{S}_\mathrm{f}(\omega) & \mathbf{0} \\ \mathbf{0} & \mathbf{0} \end{bmatrix} \tag{12}$$

which contains their respective cross-spectral densities, $S_{g,ij}(\omega)$. Equation (12) can afterwards be projected into the modal basis to get the cross-spectral density of the m-th and n-th modal state forces, which reads as follows

$$S_{p,mn}(\omega) = \sum_{i=1}^{N}\sum_{j=1}^{N} \Theta_{im}\Theta_{in}^{*} S_{f,ij}(\omega) \tag{13}$$

when the zeros in $\mathbf{S}_\mathrm{g}(\omega)$ are directly discarded.

As per Equation (10), this cross-spectral density is then multiplied by the (m,n) structural kernel

$$G_{mn}(\omega) = H_m(\omega)\, H_n^{*}(\omega) \tag{14}$$

and the (m,n) normalization constants to give

$$S_{q,mn}(\omega) = D_m D_n G_{mn}(\omega)\, S_{p,mn}(\omega) \tag{15}$$

which is the cross-spectral density of the m-th and n-th modal state responses. In the end, the cross-spectral densities of the nodal state responses can finally be obtained by recombining the modal state response spectra as such

$$S_{y,ij}(\omega) = \sum_{m=1}^{2M}\sum_{n=1}^{2M} \Theta_{im}\Theta_{in}^{*} S_{q,mn}(\omega)$$

and these functions fully describe the responses in a probabilistic sense, given that these processes inherit the zero-mean Gaussian nature of the forces when the structure is linear.

In particular, the covariance between the i-th and the j-th nodal state responses can be obtained by integrating the corresponding cross-spectrum over the frequency. In indicial formulation again, it is thus simply expressed as

$$\Sigma_{y,ij} = \sum_{m=1}^{2N}\sum_{n=1}^{2N} \Theta_{im}\Theta_{jn}^{*} \Sigma_{q,mn} \tag{16}$$

which is a linear combination of

$$\Sigma_{q,mn} = \int_{-\infty}^{+\infty} S_{q,mn}\left(\omega\right) \mathrm{d}\omega \tag{17}$$

being the covariances of the m-th and n-th modal state responses.

The integral of $S_{q,mn}\left(\omega\right)$ is, in principle, easier to compute than the integral of $S_{y,ij}\left(\omega\right)$ since it features two acute peaks at most, and no longer a multitude, which are respectively associated to the resonance of the structure in the m-th and the n-th modes, along with some strong variations related to the particular energy content of the waves, whose characteristic frequency is usually far above or far below the natural frequencies of the structure. However, despite their reduced number, the sharpness and the distinctness of the peaks imply that the integral found in Equation (17) requires a large number of closely spaced frequencies spread over a wide range for an accurate determination of the modal covariances, and thus the nodal ones.

4. Extensions of the Multiple Timescale Spectral Analysis

Whereas the sharpness and the distinctness of the peaks constitute a huge drawback for a traditional frequency domain analysis, it can in fact be turned into an advantage as it allows to use the general framework of the multiple timescale spectral analysis which has specifically been formulated to reduce drastically the number of points that are needed to compute such integrals, and especially avoid to project the cross-spectral density matrix of the forces so many times, by deriving semi-analytical approximations for their main components [12]. Coupling this approach with Giske's method [20], which provides a faster calculation for the cross-spectral densities of the nodal state loadings, should help to perform the analysis with a significantly lower computational demand.

In ocean engineering applications though, the fast dynamics are not necessarily linked with the structural motions, especially when wave-loaded structures are compliant in surge, as floating offshore wind turbines or floating bridges. Such systems might therefore respond in the background and the resonant regimes but also in the inertial one which is on the contrary hardly ever activated in land-based wind-loaded structures. In addition to the consideration of complex eigenfrequencies and eigenmodes which modify the expressions for the background and the resonant components of the modal covariances, the multiple timescale spectral analysis is also yet to take the inertial components into account. These are hence the two reasons why the method has to be extended and verified on a minimalistic example in this section before being finally applied on a more realistic wave-loaded structure in Section 5.

To illustrate these mathematical developments, the cross-spectral densities of the modal state forces are temporarily defined by using the simplified formula

$$S_{p,mn}\left(\omega\right) = P_{a,mn}\left|S_w\left(\omega\right)\right| + \mathrm{i}P_{s,mn}S_w\left(\omega\right) \tag{18}$$

presented in Appendix A while a more realistic description will be implemented later on to validate the method on a pontoon bridge. Anyways, it is interesting to notice that, after projection into a complex basis, the co- and quad-spectral densities of the modal state forces, $\Re\left[S_{p,mn}\left(\omega\right)\right]$ and $\Im\left[S_{p,mn}\left(\omega\right)\right]$, are no longer even and odd, contrary to those of real processes.

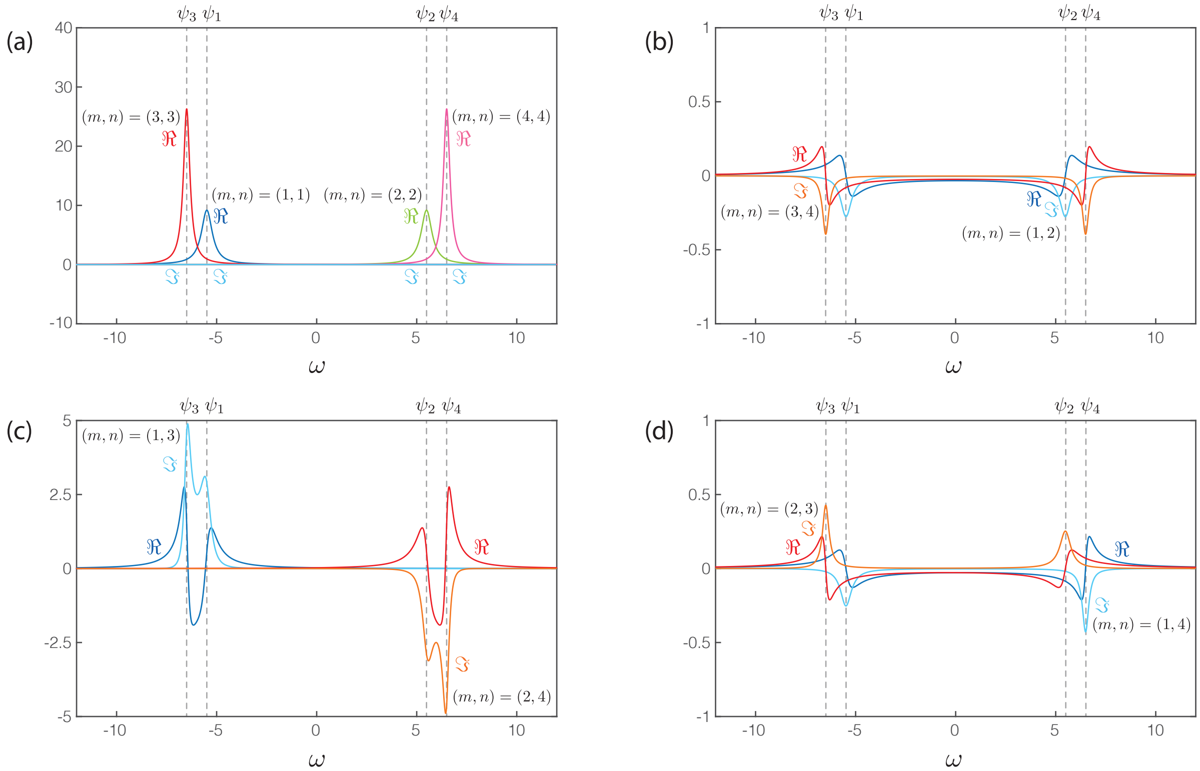

Figure 3: Real and imaginary parts of the structural kernel function when $\omega_1 = 5.5$ rad/s, $\omega_2 = 6.5$ rad/s, $\xi_1 = 0.06$, and $\xi_2 = 0.03$: (a) $|\psi_m| = |\psi_n|$ and $\psi_m\psi_n > 0$, (b) $|\psi_m| = |\psi_n|$ and $\psi_m\psi_n < 0$, (c) $|\psi_m| \neq |\psi_n|$ and $\psi_m\psi_n > 0$, (d) $|\psi_m| \neq |\psi_n|$ and $\psi_m\psi_n < 0$.

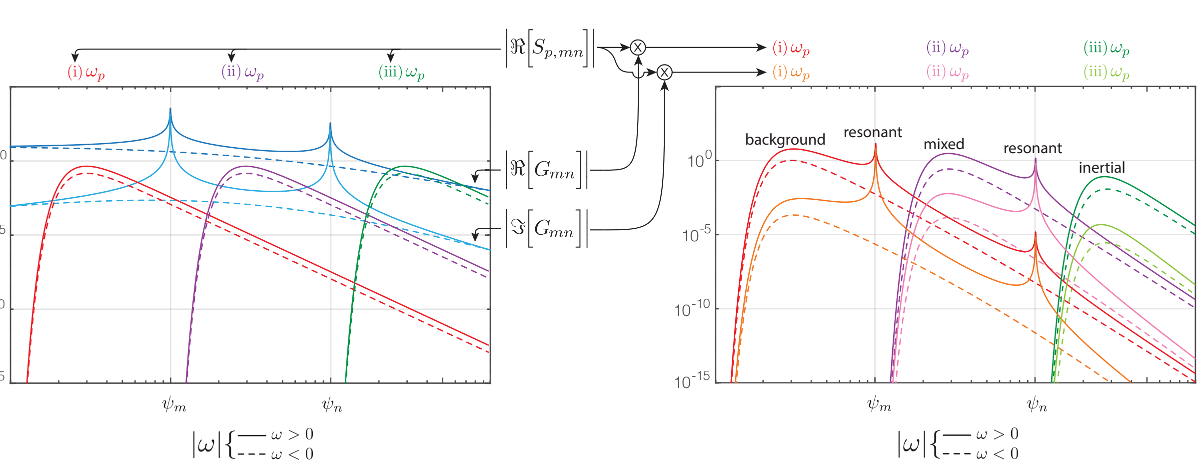

Figure 4: Origin of the peaks in the cross-spectral density of the m-th and n-th modal state responses, with m and n being even numbers. The natural frequencies and damping ratios are $\omega_{j_m} = 0.1$ rad/s, $\omega_{j_n} = 1$ rad/s, $\xi_{j_m} = 1$ % and $\xi_{j_n} = 1$ % while the cross-spectral density of the m-th and n-th modal state forces is given by Equation (18) where $P_{a,mn} = 1$, $P_{s,mn} = -\mathrm{i}/2$ and (i) $\omega_p = 0.03$ rad/s for the red and orange curves, (ii) $\omega_p = 0.3$ rad/s for the purple and pink curves or (iii) $\omega_p = 3$ rad/s for the dark and light green curves.

4.1. Preliminary Considerations and Necessary Assumptions

By looking at Figure 4, then, the major contributions to the covariance of the m-th and the n-th modal responses presented in Equation (17) are readily identified as being twofold. The first one is due to the peaks of the structural kernel and is thus called *resonant* while the second contribution comes from the peaks of the loading cross-spectrum and can therefore be named *background* if both $\omega_p < \omega_{j_m}$ and $\omega_p < \omega_{j_n}$, *inertial* if both $\omega_p > \omega_{j_m}$ and $\omega_p > \omega_{j_n}$, or *mixed* otherwise. These three cases are respectively labelled (i), (ii), and (iii) in Figure 4. Their contribution will however be referred to as the *loading component* in general.

As it is recommended in [12], these components can be evaluated sequentially by looping around the same steps: (a) select one of them, (b) find a local approximation $S_{(.),mn}(\omega)$ of the integrand $S_{q,mn}(\omega)$ that is sufficiently accurate over the corresponding peak, that is integrable in the far field, and that is simple enough to be integrated in an explicit way, (c) subtract the contribution

$$\Sigma_{(.),mn} = \int_{-\infty}^{+\infty} S_{(.),mn}(\omega)\,\mathrm{d}\omega \tag{19}$$

from $\Sigma_{q,mn}$ to obtain the remainder $\Sigma_{\tilde{q},mn} = \Sigma_{q,mn} - \Sigma_{(.),mn}$ which is actually evaluated as the integral of the residual function $S_{\tilde{q},mn}(\omega) = S_{q,mn}(\omega) - S_{(.),mn}(\omega)$. The sequence (a)-(c) is then repeated with the new integrand for the next contribution. Bit by bit, the peaks that have already been treated disappear from the residual function until a proper balance is reached between the accuracy and the complexity of the approximate formula. At this point, the iterative process is stopped and the last remainder is neglected.

In step (c), an arbitrary small parameter, $\varepsilon \ll 1$, is most often introduced together with stretched coordinates, in order to find a proper approximation for the analytical functions over the zone of interest which is justified from an asymptotic point of view. According to the perturbation theory, ε eventually disappears from the final results because it is arbitrarily chosen, even though it usually relates to a particular feature of the problem at hand.

The existence of these small numbers can typically be linked to the following assumptions, which result from the separation of timescales and ensure that the peaks of $S_{q,mn}(\omega)$ are sufficiently distinct to use the multiple timescale spectral analysis:

(i) the cross-spectral density of the loading is varying moderately over the width of the resonant peaks and this is conditioned upon the smallness of its derivatives with respect to the extent of the zone considered;

(ii) the characteristic frequency of the loading is significantly different from the characteristic frequencies of the system and this is formalized by acknowledging that the ratios

$$\alpha_m = \frac{\omega_p}{|\psi_m|} \text{ and } \alpha_n = \frac{\omega_p}{|\psi_n|} \tag{20}$$

are either much lower, either much higher, than one in absolute value.

Nevertheless, when one or both natural frequencies are close to the characteristic frequency of the waves, dropping the loading component should suffice to get a correct estimation for the covariances. Indeed, the peak of the loading cross-spectrum is stacked on one or both peaks of the structural kernel in this specific event and the resonant component is expected to encompass them all at once.

4.2. Resonant Component of the Modal State Covariances

As stated before, this first component is due to the peaks of the frequency response functions, $H_m(\omega)$ and $H_n^*(\omega)$, which can interact differently –sometimes less, sometimes more– depending on how close ψ_m is to ψ_n and eventually merge if these eigenfrequencies are coalescent, i.e. if the variance is examined $(m = n)$, see Figure 2 and Figure 3.

Fortunately enough, the structural kernel can alternatively be written

$$G_{mn}(\omega) = -\frac{H_m(\omega) - H_n^*(\omega)}{\lambda_m - \lambda_n^*} \tag{21}$$

by being expanded in partial fractions. Details about this operation are provided for the record in Appendix B even though it is actually quite straightforward to achieve because the denominator of the kernel is already factorized as the product of two first degree polynomials, $(\lambda_m - \omega)$ and $(\lambda_n^* - \omega)$, with single, whereas complex, roots in Equation (14).

As a result, the frequency response functions are subtracted from one another instead of being multiplied and the cross-spectral density of the modal responses becomes

$$S_{q,mn}(\omega) = -\frac{D_m D_n}{\lambda_m - \lambda_n^*}\left[H_m(\omega) S_{p,mn}(\omega) - H_n^*(\omega) S_{p,mn}(\omega)\right] \tag{22}$$

where the respective poles of $H_m(\omega)$ and $H_n^*(\omega)$ are now isolated in two different parts of the function to integrate without any approximation.

The stretched coordinate $\omega = \psi_m(1 + \varepsilon\eta)$ is then substituted into the first term of Equation (22) in order to focus on the pole of $H_m(\omega)$ by placing it at $\eta = 0$ and by zooming on the contributing area, where $\eta \sim \mathrm{ord}(1)$, thanks to the smallness of the arbitrary parameter, $\varepsilon \ll 1$, whose value is here related to υ_m being the half width at half height of the peak in $\Im[H_m(\omega)]$ or the half width between the positive and the negative maxima in $\Re[H_m(\omega)]$, as indicated in Figure 1-(a).

Invoking Assumption (i), the derivatives of the loading cross-spectrum are considered small enough to maintain the asymptoticness of its Taylor series expansion in the neighborhood of $\eta = 0$, or more formally $\varepsilon^i \eta^i \partial_\eta^i S_{p,mn}(\psi_m) \ll S_{p,mn}(\psi_m)$, see [12]. This cross-spectral density can therefore be replaced by the constant value $S_{p,mn}(\psi_m)$ on the region spanned by the strained coordinate while the frequency response function is expressed by

$$H_m(\eta) = -\frac{\varepsilon\eta\psi_m}{\upsilon_m^2 + (\varepsilon\eta\psi_m)^2} - \frac{\mathrm{i}\upsilon_m}{\upsilon_m^2 + (\varepsilon\eta\psi_m)^2} \tag{23}$$

which is already suitable to tackle and which is anyways not possible to simplify on the basis of the hypotheses at stake.

Following the same path for the second term of Equation (22) with another but similar stretched coordinate, $\omega = \psi_n(1 + \varepsilon\eta)$, it yields

$$S_{r,mn}(\omega) = -\frac{D_m D_n}{\lambda_m - \lambda_n^*}\left[H_m(\omega) S_{p,mn}(\psi_m) - H_n^*(\omega) S_{p,mn}(\psi_n)\right] \tag{24}$$

for approximating locally the cross-spectral density of the response over the resonant peaks. Being sufficiently simple, locally accurate and bounded in the far field, $S_{r,mn}(\omega)$ fits the requirements of the multiple timescales

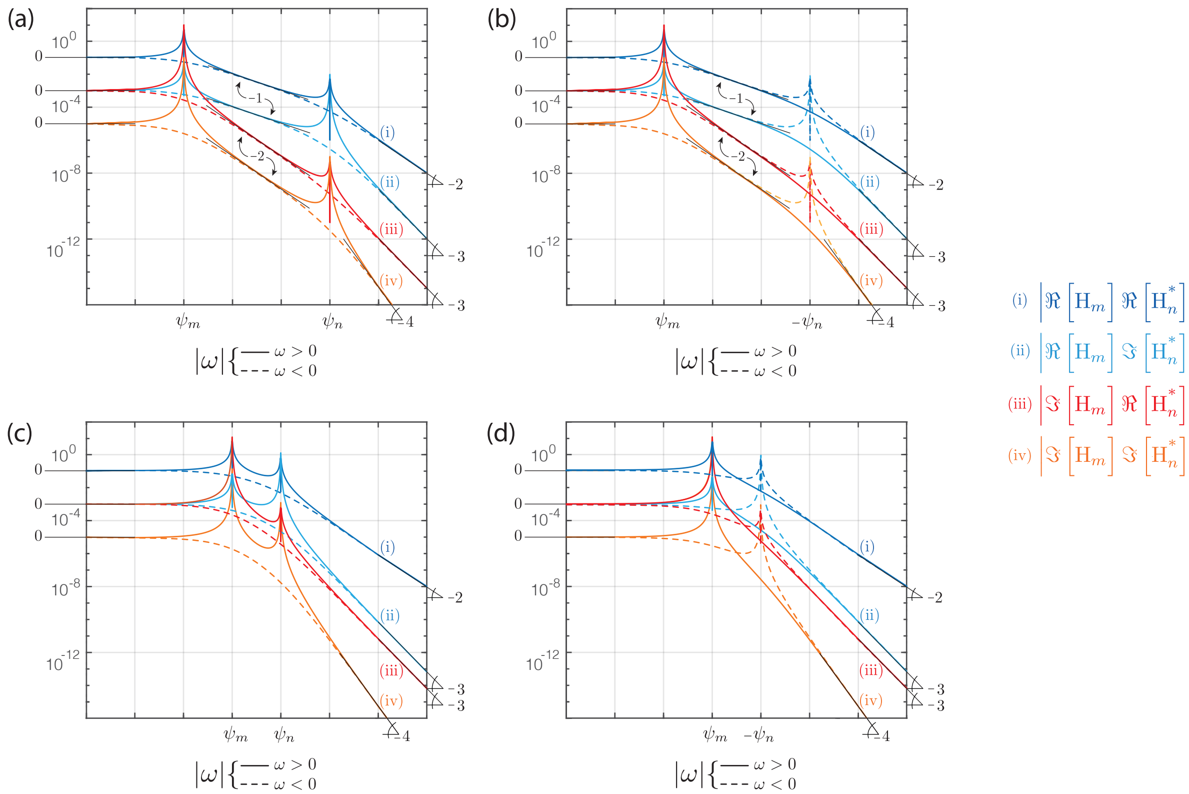

Figure 5: Decreasing trends observed in the structural kernel before, between, and after the poles of the frequency response functions: (a) $\psi_m\psi_n > 0$ and $|\psi_m| \ll |\psi_n|$, (b) $\psi_m\psi_n < 0$ and $|\psi_m| \ll |\psi_n|$, (c) $\psi_m\psi_n > 0$ and $|\psi_m| < |\psi_n|$, (d) $\psi_m\psi_n < 0$ and $|\psi_m| < |\psi_n|$

spectral analysis and can finally be integrated in an explicit way to give the resonant component of the covariance

$$\Sigma_{r,mn} = \mathrm{i}\pi \frac{D_m D_n}{\lambda_m - \lambda_n^*} \left[S_{p,mn}\left(\psi_m\right) + S_{p,mn}\left(\psi_n\right)\right] \tag{25}$$

which boils down, as expected, to the formulas derived in [9] and [12] under a few conditions, see Appendix C.

4.3. Loading Component of the Modal State Covariances

As explained in Section 4.1, Equation (25) is then subtracted from Equation (17) to give the remainder of the modal covariance

$$\Sigma_{\tilde{q},mn} = \Sigma_{q,mn} - \Sigma_{\mathrm{r},mn} \tag{26}$$

which corresponds to the integral of the residual function

$$S_{\tilde{q},mn}\left(\omega\right) = S_{q,mn}\left(\omega\right) - S_{r,mn}\left(\omega\right) \tag{27}$$

whose contribution is now solely due to the two peaks that are coming from the loading cross-spectrum. It seems important to notice that, although they are positioned symmetrically with respect to the origin (at $\omega = \pm\omega_p$), they are not supposed to reach the same maximum value.

As before, the change of coordinate $\omega = \omega_p\left(1 + \varepsilon\eta\right)$ is first introduced to focus on the peak located in the positive frequency range. Since this peak typically extends over a relatively large domain in contrast to the resonant ones, see Figure 4, the structural kernel cannot necessarily be replaced by a constant across the whole area of interest unless the background regimes are activated in both the m-th and the n-th modes. Indeed, when $\alpha_m \ll 1$ and $\alpha_n \ll 1$, the strained coordinate actually covers a domain where the frequency response functions are not varying much as $\omega_p \ll |\psi_m|$ and $\omega_p \ll |\psi_n|$, see Figure 5.

In general, instead, the real and the imaginary parts of the m-th frequency response function can conveniently be approximated by a monomial which is equal to the initial function at the considered peak location and which is characterized by the same slope in logarithmic scales. These approximations are

$$\Re\left[\tilde{H}_m(\eta)\right] = \left(\frac{1}{1+\varepsilon\eta}\right)^{\beta_m} \Re\left[H_m(0)\right] \tag{28}$$

and

$$\Im\left[\tilde{H}_m(\eta)\right] = \left(\frac{1}{1+\varepsilon\eta}\right)^{2\beta_m} \Im\left[H_m(0)\right] \tag{29}$$

where the tilde symbol is used to indicate it is an approximation and where

$$\beta_m = \left((-1)^m \alpha_m^{-1} - 1\right)^{-1} \tag{30}$$

tends to 0 or 1 respectively when $\alpha_m \ll 1$ or $\alpha_m \gg 1$, the two cases covered by Assumption (ii).

By comparing Equation (24) to Equation (22), $S_{r,mn}(\omega)$ also appears to be negligible in relation to $S_{q,mn}(\omega)$ in the region spanned by the stretched coordinate because $S_{p,mn}(\psi_m) \ll S_{p,mn}(\omega_p)$ and $S_{p,mn}(\psi_n) \ll S_{p,mn}(\omega_p)$ when the ratios α_m and α_n are either much lower, either much greater than one. If one of these inequalities is not verified, however, the loading component drops and even reaches zero in the limit case, i.e. when the cross-spectral density function is constant over the whole range of frequencies, meaning that the covariance of the modal responses is fully resonant. In order to comply with these observations while simplifying the expressions, $S_{r,mn}(\omega)$ is removed from Equation (27) and replaced by the multiplicative form

$$L_{mn} = \left(1 - \frac{S_{p,mn}(\psi_m)}{S_{p,mn}(\omega_p)}\right)\left(1 - \frac{S_{p,mn}(\psi_n)}{S_{p,mn}(\omega_p)}\right) \tag{31}$$

which accordingly decreases down to zero when a frequency or a loading cross-spectrum ratio is getting close to one.

Proceeding with the same steps for the second peak by using another but equivalent stretched coordinate, $\omega = -\omega_p(1+\varepsilon\eta)$, the local approximation of the residual function eventually reads

$$S_{\ell,mn}^{(\pm)}(\omega) = D_m D_n L_{mn} \sum_{k=1}^{4} \left[(\pm\omega_p)^{\beta_{mn}^{(k)}} \mathcal{G}_{mn}^{(k)}(\pm\omega_p)\, \mathcal{S}_{p,mn}^{(k)}(\omega)\right] \tag{32}$$

after returning to the circular frequencies. The symbols $(+)$ and $(-)$ are selected in accordance with the sign of the frequencies because of the non-symmetric nature of the peaks at stake while $\mathcal{G}_{mn}^{(k)}(\pm\omega_p)$ is defined in Table 1 and

$$\mathcal{S}_{p,mn}^{(k)}(\omega) = \omega^{-\beta_{mn}^{(k)}} S_{p,mn}(\omega) \tag{33}$$

is integrated over the positive or the negative frequency range to yield

$$\Sigma_{p,mn}^{(k)(\pm)} = \pm \int_0^{\pm\infty} \mathcal{S}_{p,mn}^{(k)}(\omega)\, \mathrm{d}\omega \tag{34}$$

Table 1: Definitions for Equations (32), (33) and (35)

k	$\beta_{mn}^{(k)}$	$\mathcal{G}_{mn}^{(k)}(\omega)$
1	$\beta_m + \beta_n$	$\Re\left[H_m(\omega)\right]\Re\left[H_n^*(\omega)\right]$
2	$\beta_m + 2\beta_n$	$\mathrm{i}\Re\left[H_m(\omega)\right]\Im\left[H_n^*(\omega)\right]$
3	$2\beta_m + \beta_n$	$\mathrm{i}\Im\left[H_m(\omega)\right]\Re\left[H_n^*(\omega)\right]$
4	$2\beta_m + 2\beta_n$	$-\Im\left[H_m(\omega)\right]\Im\left[H_n^*(\omega)\right]$

which is seen as a part of the $-\beta_{mn}^{(k)}$ spectral (fractional) moment associated to the m-th and n-th modal state forces. Interestingly enough, the integration can actually be performed in the nodal basis, before the modal projection in order to avoid doing so for the cross-spectral densities of the nodal state loadings at each integration point.

At last, the loading component of the modal covariance is given in an explicit way by

$$\Sigma_{\ell,mn} = D_m D_n L_{mn} \sum_{k=1}^{4} \left[(+\omega_p)^{\beta_{mn}^{(k)}} \mathcal{G}_{mn}^{(k)}(\omega_p) \Sigma_{p,mn}^{(k)(+)} + (-\omega_p)^{\beta_{mn}^{(k)}} \mathcal{G}_{mn}^{(k)}(\omega_p) \Sigma_{p,mn}^{(k)(-)} \right] \tag{35}$$

which boils down to the well-known background component when α_m and α_n are much lower than one ($\beta_m = \beta_n = \beta_{mn}^{(k)} = 0$). This expression however extends in a unified way to the inertial component or to mixed background/inertial covariances.

In a last step, the loading component is subtracted from Equation (26) to yield the next remainder. It can finally be neglected straightaway as it corresponds to the integral of a residual function which does no longer contain any significant contribution.

4.4. Verification of the Proposed Decomposition

To summarize, under Assumption (i) and Assumption (ii), the covariances of the m-th and n-th modal state responses can be estimated as follows

$$\Sigma_{\hat{q},mn} = \Sigma_{r,mn} + \Sigma_{\ell,mn} \tag{36}$$

where the resonant and the loading components are respectively derived in Equation (25) and Equation (35). These matrices correspond to the integral of the corresponding cross-spectral densities

$$S_{\hat{q},mn}(\omega) = S_{r,mn}(\omega) + S_{\ell,mn}^{(\pm)}(\omega) \tag{37}$$

which respectively approximate the cross-spectral density of the m-th and n-th modal state responses over the resonant and the loading peaks, see Equation (24) and Equation (32). These functions are represented at Figure 6 and Figure 7 for a few sets of parameters along with the exact cross-spectral density, which is defined in Equation (15). The good agreement illustrates the adequacy of the proposed approximation.

Likewise, Figure 8 compares the covariances obtained with the proposed expression to the reference values provided by Equation (15) where the integration is performed numerically, making use of the adaptive algorithm which is implemented in Version 12.0.0.0 of Wolfram Mathematica [27] with default parameters. Overall, they coincide quite well, except in the shaded area. A more important discrepancy is observed over there, as it was to be expected since Assumption (ii) is not verified anymore. Nevertheless, it remains reasonable thanks to the multiplicative factor L_{mn} which ensures that the background component passes by zero when $\alpha_m = 1$, or $\alpha_n = 1$, and does not grow unbounded.

On the other hand, when Assumption (ii) is met, the loading component is clearly leading over the resonant one provided that the natural frequencies of the associated modes are far away from each other as well, while the opposite occurs when these natural frequencies are close to each other as in Figure 6, for instance. This figure also shows that the interaction between the resonant peaks is conditioned upon the damping ratios. The smaller, the sharper but also the more distinct the resonant peaks. Thus, the proximity of the natural frequencies and the smallness of the damping ratios is a necessary condition for observing an acute burst in the resonant component, as shown in Figure 8-(a), but this is not sufficient, otherwise Figure 8-(b) would exhibit a similar feature.

The resonance in the m-th and n-th modes additionally needs to be activated by the loading in order to see them interacting as in Figure 6. This is however not the case if $\alpha_m \gg 1$ and $\alpha_n \gg 1$ because the resonant peaks appear in a zone where $S_{p,mn}(\psi_m)$ and $S_{p,mn}(\psi_n)$ are exponentially small as a result of the exponential decay displayed by the loading cross-spectral density when the frequencies are getting much lower than the peak frequency. This is also the reason why one, or both, resonant peaks respectively disappear from Figure 7-(b) and Figure 7-(a).

Apart from that, in Figure 8, the loading component tends towards zero (resp. a non-zero constant value) when α_n is far below one (resp. far above one) because α_m and thus $H_m(\pm\omega_p)$ are fixed while ψ_n increases (resp. decreases) and eventually leads over ω_p (resp. becomes negligible in relation to ω_p) in $H_n^*(\pm\omega_p)$ which is hence dropping towards zero (resp. stabilizing at a constant value) as well.

5. Case Study: the Bergsøysund Bridge

The approximate formulations roposed in Section 4 are now validated on a simplified 2D model, considering the horizontal displacements and rotations only. This example is inspired by the Bergsøysund Bridge which crosses a 100-m deep strait in Norway and is one of the longest end-anchored floating bridges in the world with its total length of 933 m. As shown in Figure 9, it is composed of 7 pontoons linked together by steel truss segments of 105 m long, which are modelled as single equivalent beams with 10 elements of equal length by section for the sake of the illustration in this paper.

Their properties are given in Table 2 and have been chosen, regardless of realisticness, to illustrate the capabilities of the proposed formulation, by activating all possible combinations of responses in the background and the inertial regimes. The resulting natural frequencies, damping ratios and mode shapes are listed in Table 3. For the same reason, the pontoons and the forces are defined as in [28] but using as the one-dimensional wave spectral density a two-parameter Pierson-Moskovitz spectrum

$$S_{pm}(\omega) = \frac{5h_s}{16\omega_p}\left(\frac{\omega_p^5}{\omega^5}\right)\exp\left(-\frac{5}{4}\frac{\omega_p^4}{\omega^4}\right) \tag{38}$$

with $h_s = 2.4$ m being the significant wave height and $\omega_p = 2.2$ rad/s being the peak frequency at which the hydrodynamic matrices are evaluated, as explained in Section 3. A spreading parameter of 3 is also selected because it allows to neglect the correlations between the forces applied on different pontoons.

The power and cross-spectral densities of the modal state responses appear to be correctly approximated by the proposed formulation, see Figure 10 and Figure 11, respectively. In Figure 10-(a) and Figure 11-(a), the modal responses are activated in their inertial regime by the loading. The resonant components consequently disappear, as in Section 4.4, due to the particular shape of the loading spectra in the low frequencies.

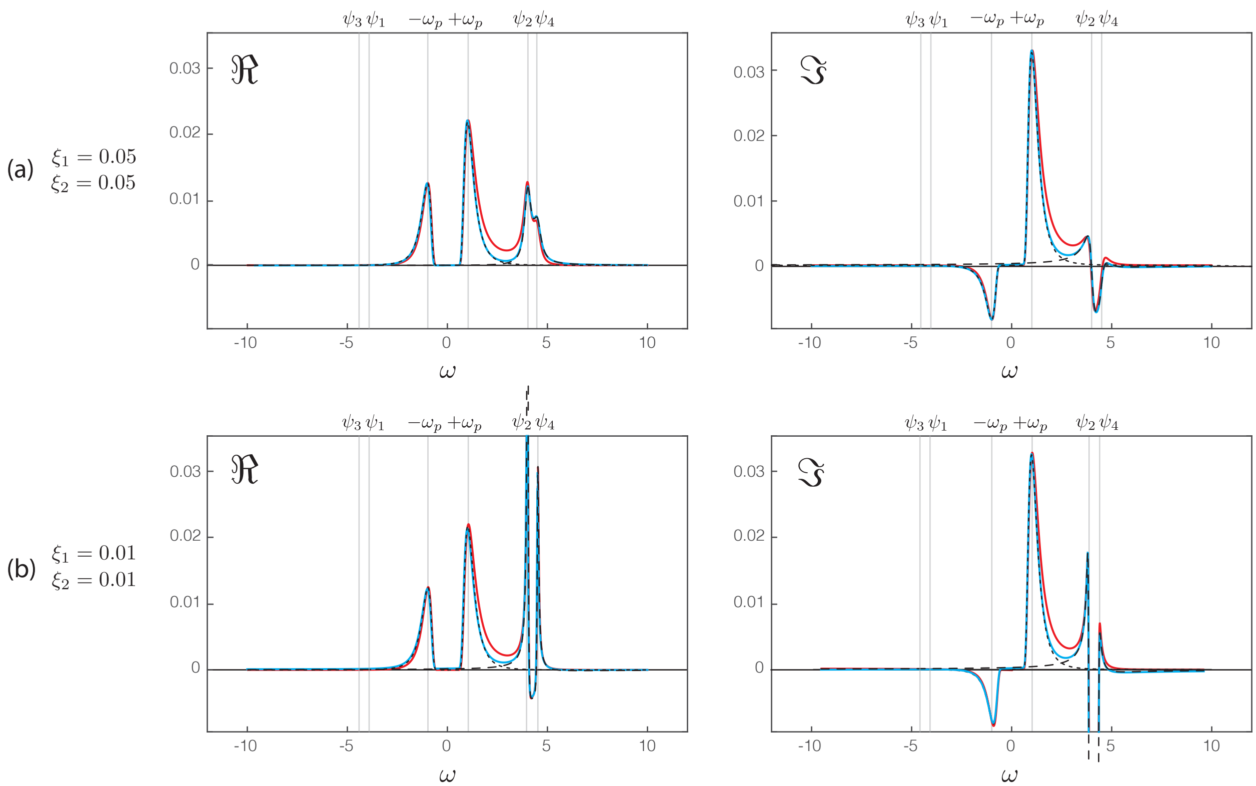

Figure 6: Cross-spectral densities of the 2[nd] and 4[th] modal state responses together with the local approximations provided for the resonant and the loading components when $P_a = (1 + 0.2\mathrm{i})$, $P_s = (\mathrm{i} - 0.2)$, $\omega_1 = 4$ rad/s and $\omega_2 = 4.5$ rad/s while (a) $\xi_1 = 5$ % and $\xi_2 = 5$ % or (b) $\xi_1 = 1$ % and $\xi_2 = 1$ %. Red lines illustrate the reference function, $S_{q,mn}(\omega)$. Blue lines represent the proposed approximation, $S_{\hat{q},mn}(\omega)$. Dashed and dotted lines respectively correspond to the resonant and the loading components, $S_{r,mn}(\omega)$ and $S^{(\pm)}_{\ell,mn}(\omega)$. Notice that their lack of symmetry properties is due to use of complex mode shapes.

Parameter	Value [unit]
Length	10.5 [m]
Moment of Inertia	12.36 [m^4]
Young Modulus	2.10^{10} [N/m^2]
Cross-Section	0.6 [m^2]
Density	7850 [kg/m^3]

Table 2: Geometric and material parameters of the bridge model.

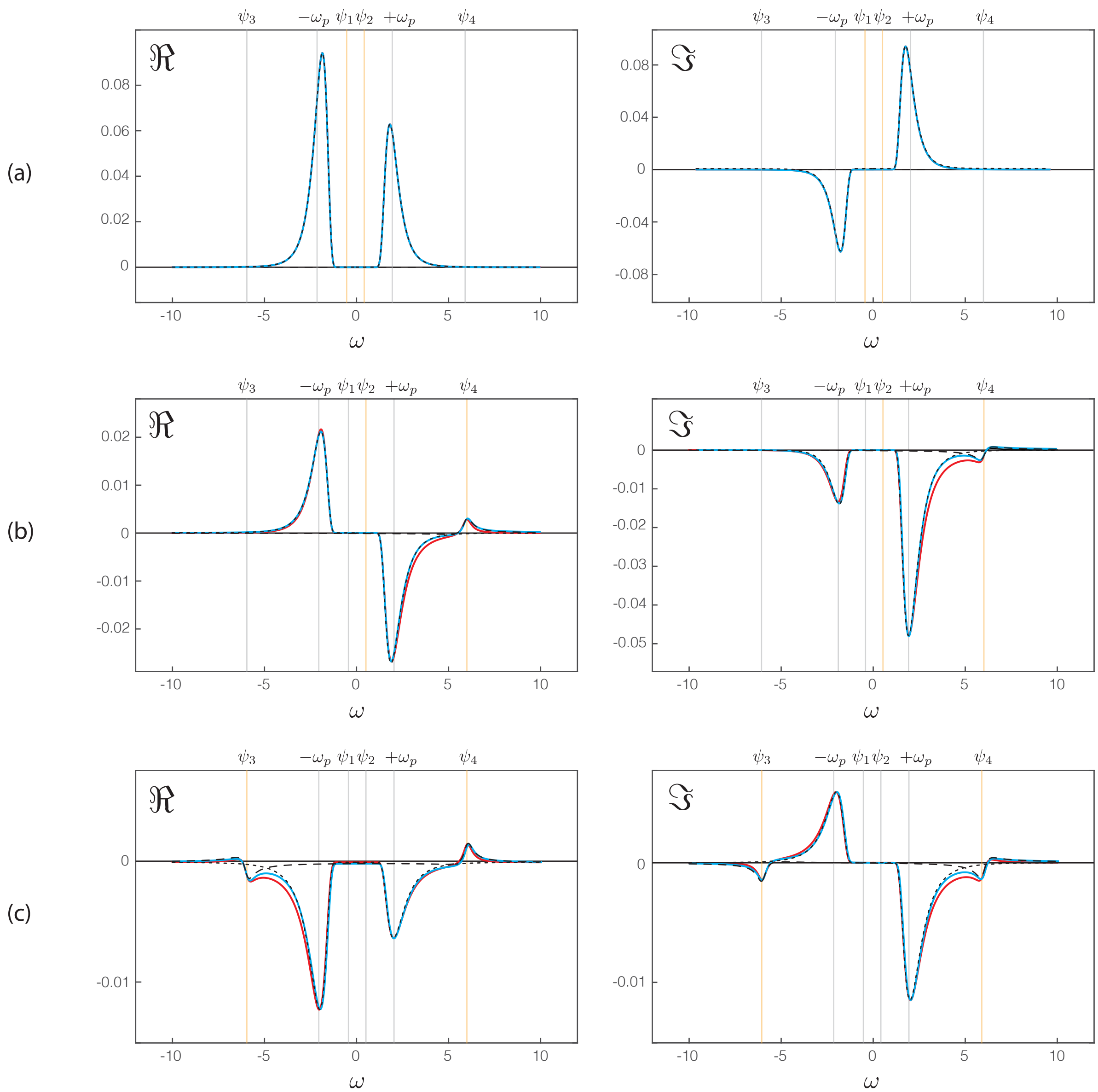

Figure 7: Cross-spectral densities of the m-th and n-th modal state responses together with the local approximations provided for the resonant and the loading components when $P_a = (1 + 0.2\mathrm{i})$ and $P_s = (\mathrm{i} - 0.2)$ for all (m, n) pairs indicated by yellow lines while $\omega_1 = 0.1$ rad/s and $\omega_2 = 6$ rad/s. Red lines illustrate the reference function, $S_{q,mn}(\omega)$. Blue lines represent the proposed approximation, $S_{\hat{q},mn}(\omega)$. Dashed and dotted lines respectively correspond to the resonant and the loading components, $S_{r,mn}(\omega)$ and $S^{(\pm)}_{\ell,mn}(\omega)$. Notice that their lack of symmetry properties is due to use of complex mode shapes.

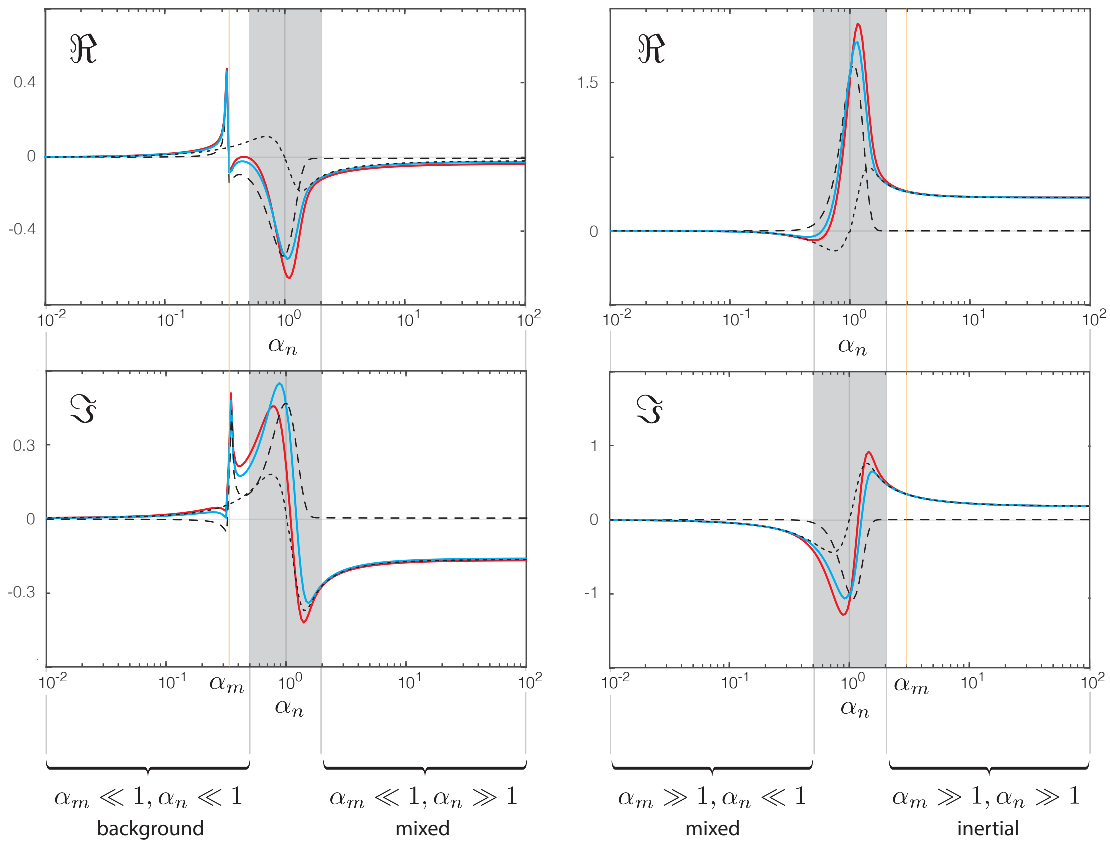

Figure 8: Covariances of the m-th and n-th modal state responses, with m and n being even numbers, when $\xi_{j_m} = 1$ %, $\xi_{j_n} = 1$ %, $P_a = (1 + 0.2\mathrm{i})$, $P_s = (\mathrm{i} - 0.2)$, and $\omega_p = 1$ rad/s while (a) $\alpha_m = 0.3$ and (b) $\alpha_m = 3$. Red lines illustrate the reference results, $S_{q,mn}(\omega)$. Blue lines represent the proposed approximation, $S_{\hat{q},mn}(\omega)$. Dashed and dotted lines respectively correspond to the resonant and the loading components, $S_{r,mn}(\omega)$ and $S_{\ell,mn}^{(\pm)}(\omega)$. Notice that their lack of symmetry properties is due to use of complex mode shapes.

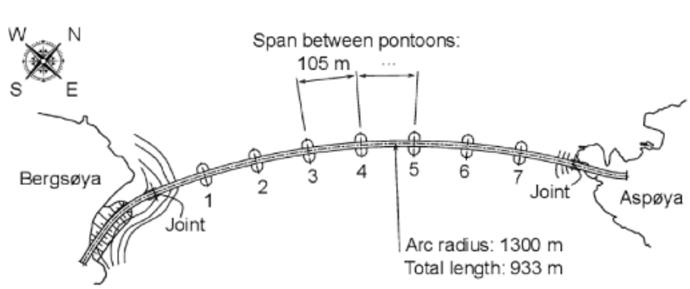

Figure 9: Top view of the Bergsøysund Bridge.

j_m	ω_{j_m} [rad/s]	ξ_{j_m} [%]	Mode Shape
1	0.27	16.5	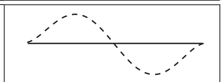
2	0.42	10.1	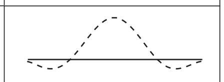
3	0.68	5.93	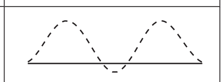
4	0.88	5.27	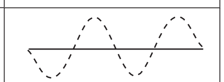
5	1.32	3.64	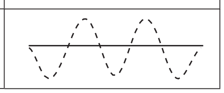
6	1.77	2.78	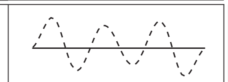
7	2.07	2.19	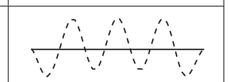
8	2.73	5.58	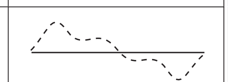
9	3.21	2.84	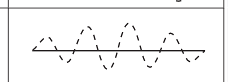
10	3.75	2.65	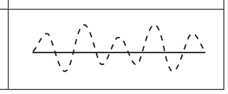
11	4.32	2.51	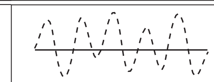
12	4.85	2.38	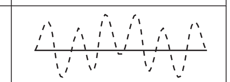
13	5.33	2.28	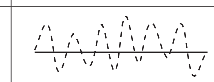
14	5.51	2.56	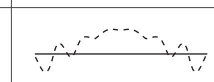
15	5.77	2.36	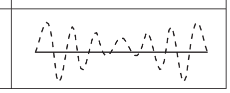

Table 3: Modal analysis of the bridge model.

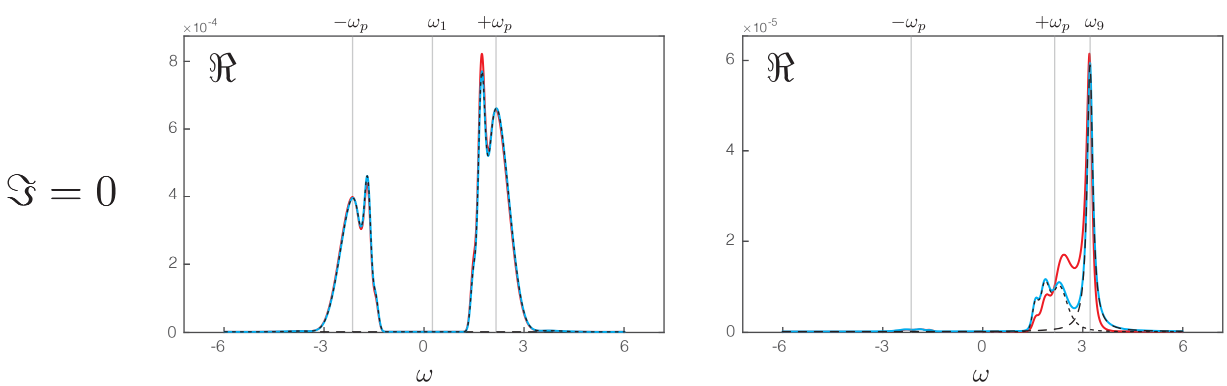

Figure 10: Power spectral densities of the m-th modal state responses together with the local approximations provided for the resonant and the loading components when $m = 2$ (left) and $m = 18$ (right). Red lines illustrate the reference function, $S_{q,mm}(\omega)$. Blue lines represent the proposed approximation, $S_{\hat{q},mm}(\omega)$. Dashed and dotted lines respectively correspond to the resonant and the loading components, $S_{r,mm}(\omega)$ and $S^{(\pm)}_{\ell,mm}(\omega)$. Notice that their lack of symmetry properties is due to use of complex mode shapes.

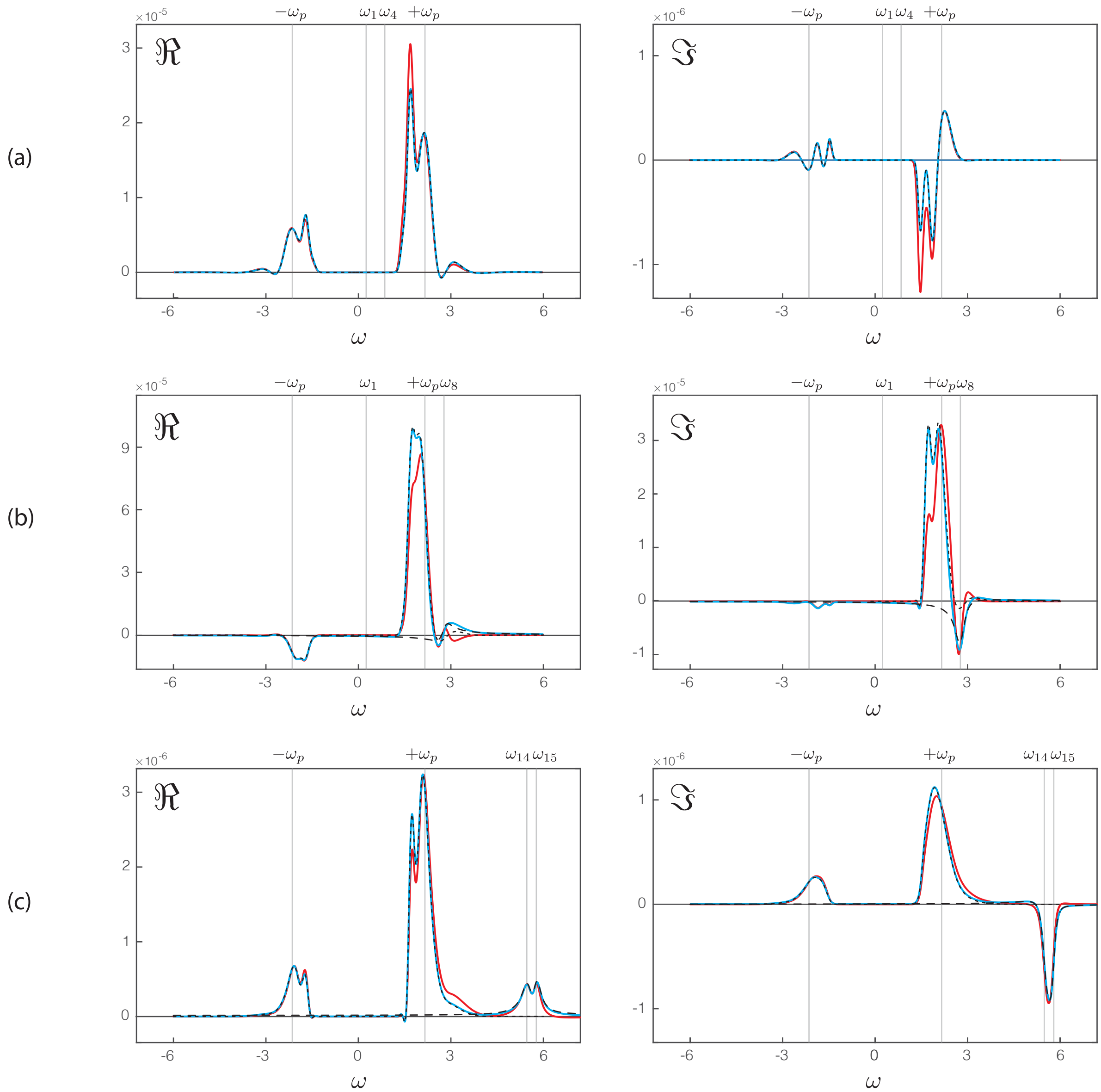

Figure 11: Cross-spectral densities of the m-th and n-th modal state responses together with the local approximations provided for the resonant and the loading components when (a) $m = 2$ and $n = 8$, (b) $m = 2$ and $n = 16$, (c) $m = 28$ and $n = 30$. Red lines illustrate the reference function, $S_{q,mn}(\omega)$. Blue lines represent the proposed approximation, $S_{\hat{q},mn}(\omega)$. Dashed and dotted lines respectively correspond to the resonant and the loading components, $S_{r,mm}(\omega)$ and $S^{(\pm)}_{\ell,mm}(\omega)$. Notice that their lack of symmetry properties is due to use of complex mode shapes.

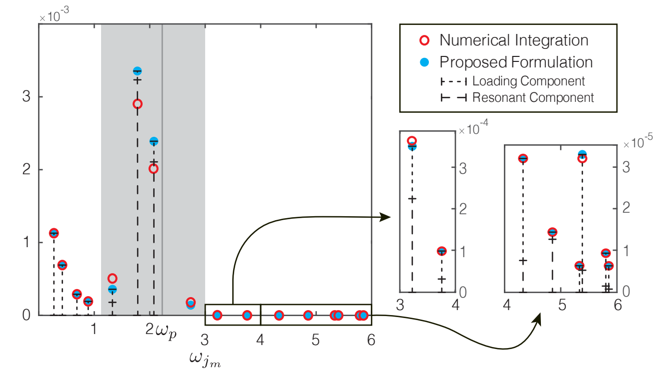

Figure 12: Variances of the modal state responses for the bridge model presented in this section. Red circles illustrate the reference results, $\Sigma_{q,mm}$. Blue dots represent the proposed approximation, $\Sigma_{\hat{q},mm}$. Dashed and dotted lines respectively correspond to the resonant and the loading components, $\Sigma_{r,mm}$ and $\Sigma_{\ell,mm}$.

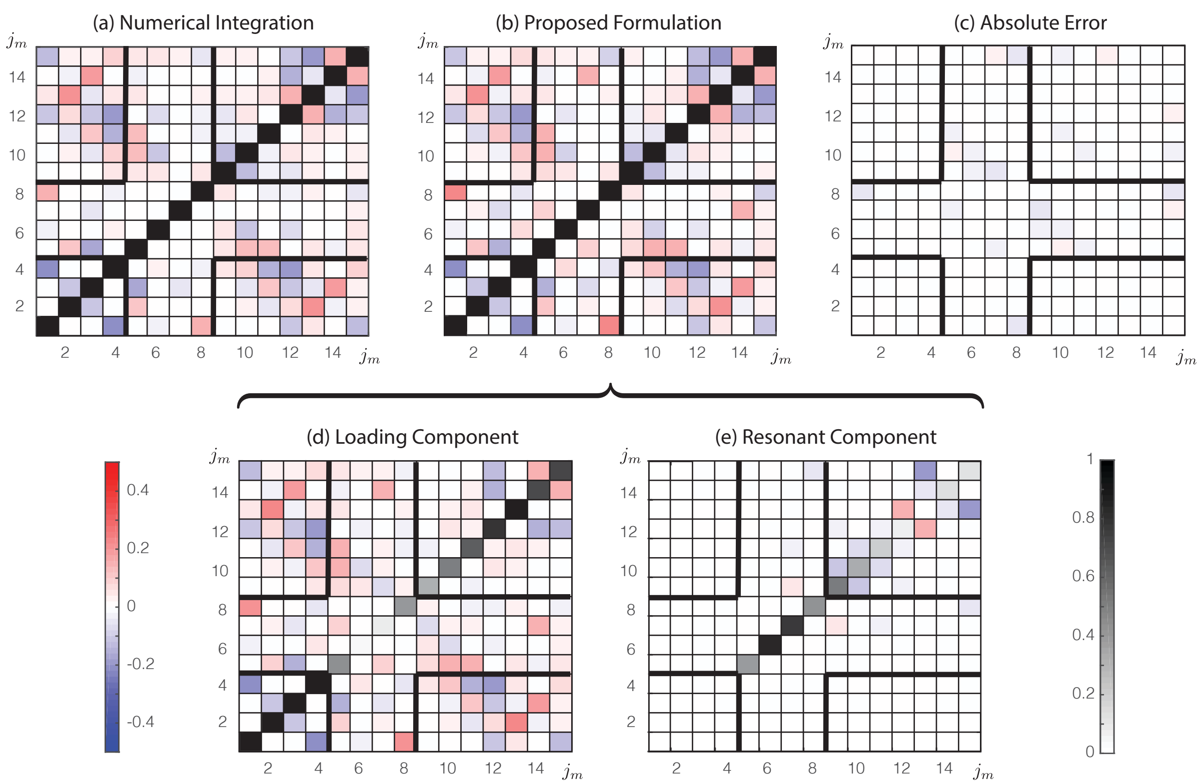

Figure 13: Correlation coefficients of the modal state responses for the bridge model: (a) results obtained with the numerical integration (b) results obtained with the proposed approximation, (c) absolute errors between the former results, (d) the loading components and (e) the resonant components. Diagonal elements in greyscale color represent the weighting factors, γ_ℓ and γ_r.

Besides, Figure 12 compares the modal state variances computed by means of the proposed approximation to the values obtained by integrating numerically the power spectral densities given in Equation (15) when $m = n$. Globally, they agree quite well, except in the shaded area where a larger discrepancy is observed again because Assumption (ii) is not respected. Contrary to what the figure suggests, the responses in these modes are actually neither mainly resonant, neither loading driven but the timescales associated to each of these two phenomena are interacting.

Being nondimensional and bounded in the interval $[-1, 1]$, the correlation coefficients are more appropriate to assess the importance of taking a specific modal state covariance into account. Details about their derivation are given in Appendix D. The results obtained with the numerical integration are represented together with the results obtained with the proposed approximation in Figure 13-(a) and Figure 13-(b), respectively. Figure 13-(c) then shows the absolute error committed between the former and the latter while Figure 13-(d) and 13-(e) illustrate the decomposition of the latter into the loading and the resonant component.

On each of these subfigures, the coefficients are divided into five categories and said partly inertial in the bottom-left corners, partly background in the top-right corners, and partly mixed in the two remaining corners, bottom-right and top-left, while the loading and resonant peaks interact in the cross-shaped areas. Just as before, a good match is observed, with a bit less accuracy in the central zone, between the approximated and the reference values. Meanwhile, the computational time has been divided by 20. The proposed approximation is thus shown to provide an interesting balance between precision and efficiency.

Finally, although the modal correlations are often related to the interactions between the resonance in two different modes and neglected provided that their natural frequencies are sufficiently distant from each other as it is confirmed by looking at Figure 13-(e), they also appear to be significantly influenced by the loading components, see Figure 13-(d). They should especially be important when the m-th and n-th modal forces are coherent, which happens when the m-th and n-th mode shapes are similar. The 1$^{\text{st}}$ and 8$^{\text{th}}$ modes, for instance, are both symmetric, changing sign at mid-length and possessing two half waves.

6. Conclusions

The multiple timescale spectral analysis is implemented in this paper to derive semi-analytical approximations for computing more efficiently the variances and the covariances of modal state responses. As a result, they are obtained by summing two component with easily understandable expressions: the resonant and the loading component. The former component requires to determine the cross-spectral densities of the modal state loadings at the natural frequencies of the structure only while the latter component is based on a few of their spectral moments. These statistics can actually be evaluated by integrating the loading spectra in the nodal basis first. The few matrices they constitute can then be projected into the modal basis. It thus avoids to do so with the loading spectra for all the numerous points of integration.

All in all, it means that the proposed formulation drastically reduces the number of frequencies at which the cross-spectral densities of the nodal state loadings have to be projected. In addition to being simple, it thus provides accurate results in a significantly lower computational time. In this paper, for instance, it has been benchmarked against the heavy integration of the response spectra for a low-dimensional model inspired by the Bergsøysund

Bridge. The analysis appeared to be performed 20 times faster without sacrificing accuracy and this computational speed up is expected to be even larger for models with up to several thousands degrees-of-freedom.

7. References

References

[1] S. Adhikari. Damping modelling using generalized proportional damping. *Journal of Sound and Vibration*, 293(1-2):156–170, 2006.

[2] Yong Bai. *Marine structural design*. Elsevier, 2003.

[3] Nigel D P Barltrop and Adrian J Adams. *Dynamics of fixed marine structures*, volume 91. Butterworth-Heinemann, 2013.

[4] Michael Borg, Lance Manuel, Maurizio Collu, and Jinsong Liu. Long-term global performance analysis of a vertical-axis wind turbine supported on a semi-submersible floating platform. In *International Conference on Offshore Mechanics and Arctic Engineering*, volume 56574, page V009T09A066. American Society of Mechanical Engineers, 2015.

[5] T. K. Caughey and M. E. O'Kelly. Classical normal modes in damped linear dynamic systems. *Journal of Applied Mechanics, Transactions ASME*, 32(3):583–588, 1965.

[6] Subrata Kumar Chakrabarti. *Hydrodynamics of offshore structures*. WIT press, 1987.

[7] A. G. Davenport. The spectrum of horizontal gustiness near the ground in high winds. *Quarterly Journal of the Royal Meteorological Society*, 87(372):194–211, 1961.

[8] Shi Deng, Yuwang Xu, Haojie Ren, Shixiao Fu, Shuai Li, Torgeir Moan, and Zhen Gao. Numerical simulation of wave-induced hydroelastic response and flow-induced vibration of a twin-tube submerged floating tunnel. *Marine Structures*, 82(September 2021):103124, 2022.

[9] V. Denoël. Estimation of modal correlation coefficients from background and resonant responses. *Structural Engineering and Mechanics*, 32(6):725–740, 2009.

[10] V. Denoël. On the background and biresonant components of the random response of single degree-of-freedom systems under non-Gaussian random loading. *Engineering Structures*, 33(8):2271–2283, 2011.

[11] V. Denoël. Multiple timescale spectral analysis of a linear fractional viscoelastic system under colored excitation. *Probabilistic Engineering Mechanics*, 53(May):66–74, 2018.

[12] Vincent Denoël. Multiple timescale spectral analysis. *Probabilistic Engineering Mechanics*, 39:69–86, 2015.

[13] Vincent Denoël and Luigi Carassale. Response of an oscillator to a random quadratic velocity-feedback loading. *Journal of Wind Engineering and Industrial Aerodynamics*, 147:330–344, 2015.

[14] Jun Ding, Yousheng Wu, Zhuoyu Xie, Weinan Yang, Siyu Wang, Jun Yu, and Tao Yu. Overview: Research on hydroelastic responses of VLFS in complex environments. *Marine Structures*, 78(March):102978, 2021.

[15] O. M. Faltinsen. Sea Loads on Ships and Offshore Structures, 1990.

[16] K. A. Foss. Co-ordinates which uncouple the equations of motion of a damped linear systems. *Journal of Applied Mechanics*, 25(May):361–364, 1967.

[17] Finn-Idar G Giske, Bernt Johan Leira, and Ole Øiseth. Long-term extreme response analysis of marine structures using inverse SORM. *Journal of Offshore Mechanics and Arctic Engineering*, 140(5), 2018.

[18] Finn Idar Grøtta Giske, Knut Andreas Kvåle, Bernt Johan Leira, and Ole Øiseth. Long-term extreme response analysis of a long-span pontoon bridge. *Marine Structures*, 58(December 2017):154–171, 2018.

[19] Finn-Idar Grøtta Giske, Bernt Johan Leira, and Ole Øiseth. Stochastic Modelling of Wave Loads on Floating Bridges : Efficient Calculation of Cross-Spectral Densities. *19th Congress of IABSE, Challenges in Design and Construction of an Innovative and Sustainable Built Environment*, (September):48–56, 2016.

[20] Finn-Idar Grøtta Giske, Bernt Johan Leira, and Ole Øiseth. Efficient computation of cross-spectral densities in the stochastic modelling of waves and wave loads. *Applied Ocean Research*, 62:70–88, 2017.

[21] Finn-Idar Grøtta Giske, Bernt Johan Leira, and Ole Øiseth. Full long-term extreme response analysis of marine structures using inverse FORM. *Probabilistic Engineering Mechanics*, 50:1– 8, 2017.

[22] Odin Gramstad, Christian Agrell, Elzbieta Bitner-Gregersen, Bingjie Guo, Eivind Ruth, and Erik Vanem. Sequential sampling method using Gaussian process regression for estimating extreme structural response. *Marine Structures*, 72:102780, 2020.

[23] Ming Gu and Xuan yi Zhou. An approximation method for resonant response with coupling modes of structures under wind action. *Journal of Wind Engineering and Industrial Aerodynamics*, 97(11-12):573–580, 2009.

[24] Julien Heremans, Anass Mayou, and Vincent Denoël. Background/Resonant decomposition of the stochastic torsional flutter response of an aeroelastic oscillator under buffeting loads. *Journal of Wind Engineering and Industrial Aerodynamics*, 208(July), 2021.

[25] E.J. Hinch. *Perturbation Methods*. Cambridge University Press, Cambridge, 1995.

[26] A. Ibrahimbegovic and E. L. Wilson. Simple numerical algorithms for the mode superposition analysis of linear structural systems with non-proportional damping. *Computers and Structures*, 33(2):523–531, 1989.

[27] Wolfram Research, Inc. Mathematica, Version 12.0, 2019. Champaign, IL.

[28] Knut Andreas Kvåle, Ragnar Sigbjörnsson, and Ole Øiseth. Modelling the stochastic dynamic behaviour of a pontoon bridge: A case study. *Computers and Structures*, 165:123–135, 2016.

[29] Curtis E Larsen and Loren D Lutes. Predicting the fatigue life of offshore structures by the single-moment spectral method. In *Stochastic Structural Dynamics 2*, pages 91–120. Springer, 1991.

[30] Tor M Lystad, Aksel Fenerci, and Ole Øiseth. Long-term extreme buffeting response of cable-supported bridges with uncertain turbulence parameters. *Engineering Structures*, 236:112126, 2021.

[31] F M Mazzolani, R Landolfo, B Faggiano, M Esposto, Federico Perotti, and Gianluca Barbella. Structural analyses of the submerged floating tunnel prototype in Qiandao Lake (PR of China). *Advances in structural engineering*, 11(4):439–454, 2008.

[32] Torgeir Moan and Mathias Egeland Eidem. Floating bridges and submerged tunnels in Norway - the history and future outlook. In *WCFS2019*, pages 81–111. Springer, 2020.

[33] Arvid Naess and Torgeir Moan. *Stochastic dynamics of marine structures.* Cambridge University Press, 2013.

[34] M. Palmieri, F. Cianetti, G. Zucca, G. Morettini, and C. Braccesi. Spectral analysis of sine-sweep vibration: A fatigue damage estimation method. *Mechanical Systems and Signal Processing*, 157:107698, 2021.

[35] B. N. Parlett and H. C. Chen. Use of indefinite pencils for computing damped natural modes. *Linear Algebra and Its Applications*, 140(C):53–88, 1990.

[36] Joseph Penzien and Ray W. Clough. Dynamics of structures. *Earthquake Engineering Handbook*, pages 3–1–3–40, 2002.

[37] X. Pitoiset and A. Preumont. Spectral methods for multiaxial random fatigue analysis of metallic structures. *International Journal of Fatigue*, 22(7):541–550, 2000.

[38] Ragnar Sigbjörnsson. Stochastic theory of wave loading processes. *Engineering Structures*, 1:58–64, 1979.

[39] Reza Taghipour, Tristan Perez, and Torgeir Moan. Hybrid frequency-time domain models for dynamic response analysis of marine structures. *Ocean Engineering*, 35(7):685–705, 2008.

[40] Françoise Tisseur. Backward error and condition of polynomial eigenvalue problems. *Linear Algebra and Its Applications*, 309(1-3):339–361, 2000.

[41] C. M. Wang and B. T. Wang. *Large Floating Structures.* 2015.

[42] E. Watanabe, T. Utsunomiya, and C. M. Wang. Hydroelastic analysis of pontoon-type VLFS: A literature survey. *Engineering Structures*, 26(2):245–256, 2004.

[43] E Watanabe, C M Wang, T Utsunomiya, and T Moan. Very large floating structures: applications, analysis and design. *Core report of centre for offshore research and engineering national university of Singapore*, (2):1–30, 2004.

[44] Eiichi Watanabe. Floating bridges: past and present. *Structural engineering international*, 13(2):128–132, 2003.

[45] Yuwang Xu, Aksel Fenerci, Ole Øiseth, and Torgeir Moan. Efficient prediction of wind and wave induced long-term extreme load effects of floating suspension bridges using artificial neural networks and support vector machines. *Ocean Engineering*, 217:107888, 2020.

[46] Olgierd Cecil Zienkiewicz, Robert Leroy Taylor, Perumal Nithiarasu, and J Z Zhu. *The finite element method*, volume 3. McGraw-hill London, 1977.

8. Acknowledgements

The financial support of a FRIA Fellowship granted by the F.R.S.-FNRS (the Belgian Fund for Scientific Research) is gratefully acknowledged by the first author. Part of this research has also been conducted during her stay at NTNU Trondheim which was partially funded by a Research Stay Grant awarded by the Federation Wallonia-Brussels, a District Grant attributed by the Rotary Club of Seraing and a Scientific Mission Subsidy received from the University of Liège.

Appendix A: Simple Expression for the Loading Spectra

As explained in Section 3, the autospectral density found in Equation (**??**) is commonly multiplied by a few other functions of the circular frequencies to include effects which are due to directional spreading, amplitude operators, or spatial correlations. But these additional frequency dependencies can first be discarded to get a simple expression for the cross-spectral densities of the forces. To illustrate the mathematical developments in Section 4, they are thus temporarily written

$$\mathbf{S}_{\mathrm{f}}(\omega) = \mathbf{F}_{\mathrm{a}} \left| S_w(\omega) \right| + \mathrm{i}\mathbf{F}_{\mathrm{s}} S_w(\omega)$$

where the coefficients in the matrices $\mathbf{F}_{\mathrm{a}}$ and $\mathbf{F}_{\mathrm{s}}$ are chosen as constant, real and such that $\mathbf{F}_{\mathrm{a}} = \mathbf{F}_{\mathrm{a}}^{\intercal}$ and $\mathbf{F}_{\mathrm{s}} = -\mathbf{F}_{\mathrm{s}}^{\intercal}$ in order to ensure that the cross-spectral densities verify the following properties

$$\begin{cases} \Re\left[S_{f,mn}(\omega)\right] = +\Re\left[S_{f,mn}(-\omega)\right] \\ \Im\left[S_{f,mn}(\omega)\right] = -\Im\left[S_{f,mn}(-\omega)\right] \end{cases} \tag{39}$$

and

$$S_{f,mn}(\omega) = S^*_{f,mn}(\omega)$$

according to [38]. In particular, the power spectral densities obtained when $m = n$ are real and positive over the whole range of circular frequencies, as it is usual with actual loading processes, since the diagonal elements of the matrix $\mathbf{F}_{\mathrm{s}}$ are all equal to zero when $\mathbf{F}_{\mathrm{s}} = -\mathbf{F}_{\mathrm{s}}^{\intercal}$. After projection in the modal basis, it gives

$$\mathbf{S}_{\mathrm{p}}(\omega) = \mathbf{P}_{\mathrm{a}} \left| S_w(\omega) \right| + \mathrm{i}\mathbf{P}_{\mathrm{s}} S_w(\omega) \tag{40}$$

where

$$\mathbf{P}_{\mathrm{a}} = \mathbf{\Theta}^{\intercal}\mathbf{F}_{\mathrm{a}}\mathbf{\Theta}^* \text{ and } \mathbf{P}_{\mathrm{s}} = \mathbf{\Theta}^{\intercal}\mathbf{F}_{\mathrm{s}}\mathbf{\Theta}^*$$

are now filled with complex entries, such that $\mathbf{P}_{\mathrm{a}} = \mathbf{P}_{\mathrm{a}}^{\dagger}$ and $\mathbf{P}_{\mathrm{s}} = -\mathbf{P}_{\mathrm{s}}^{\dagger}$. It implies that the symmetry properties listed hereabove do not stand for the generalized cross-spectral densities because their real and imaginary parts respectively read

$$\begin{cases} \Re\left[\mathbf{S}_{\mathrm{p}}(\omega)\right] = \Re\left[\mathbf{P}_{\mathrm{a}}\right] \left| S_w(\omega) \right| - \Im\left[\mathbf{P}_{\mathrm{s}}\right] S_w(\omega) \\ \Im\left[\mathbf{S}_{\mathrm{p}}(\omega)\right] = \Im\left[\mathbf{P}_{\mathrm{a}}\right] \left| S_w(\omega) \right| + \Re\left[\mathbf{P}_{\mathrm{s}}\right] S_w(\omega) \end{cases}$$

and are given by the sum of symmetric and anti-symmetric functions of the circular frequencies.

Appendix B: Partial Decomposition of the Structural Kernel

The denominator of $G_{mn}(\omega)$ is already factorized as the product of the first degree polynomials $(\lambda_m - \omega)$ and $(\lambda_n^* - \omega)$. Its partial decomposition is thus expected to read

$$G_{mn}(\omega) = \frac{a}{(\lambda_m - \omega)} + \frac{b}{(\lambda_n^* - \omega)} \tag{41}$$

where a and b are constant but complex coefficients. Equation (41) can be solved for b as follows

$$b = \frac{1 - a\,(\lambda_n^* - \omega)}{(\lambda_m - \omega)} \tag{42}$$

and the subsequent replacement of ω by λ_n^* in this expression yields

$$b = \frac{1}{(\lambda_m - \lambda_n^*)} \tag{43}$$

which is then reintroduced into Equation (42) to get

$$a = -b \tag{44}$$

after some algebra.

These two coefficients are substituted back in the initial equation and the partial decomposition of the structural kernel is eventually given by

$$G_{mn}(\omega) = -\frac{1}{\lambda_m - \lambda_n^*}\left[\frac{1}{(\lambda_m - \omega)} - \frac{1}{(\lambda_n^* - \omega)}\right] \tag{45}$$

or equivalently by

$$G_{mn}(\omega) = -\frac{H_m(\omega) - H_n^*(\omega)}{\lambda_m - \lambda_n^*} \tag{46}$$

in terms of the frequency response functions.

Appendix C: Specialization of the Proposed Formulation to Former Approximations

The additional assumptions formulated in [9] and [12] are sequentially implemented in Equation (25) to recover the approximations that have already been developed in more restrictive circumstances for the resonant component of the covariance between the responses in two different modes and finally end up with the well-known expression coming from the background-resonant decomposition of Davenport for the specific case of the variance. All in all, the demonstration provided hereafter aims at confirming that the formula derived in this paper is in fact more general and can be used in an even broader domain of application. To this aim, odd m and n indices are considered in order to look at similar cases as in [12] and [7] where the contributions of the resonant peaks located in the positive frequency range are analyzed. The results are then multiplied by 2 in order to account for the peaks situated in the negative frequency range as well.

1. The off-diagonal terms of the modal damping matrix are neglected.

As a result,

$$\begin{cases} \boldsymbol{\phi}_m = \boldsymbol{\varphi}_{j_m} & \text{when } m \text{ is odd} \\ \boldsymbol{\phi}_m = -\mathrm{i}\boldsymbol{\varphi}_{j_m}^* & \text{when } m \text{ is even} \end{cases}$$

where $\boldsymbol{\phi}_m$ is the top half part of $\boldsymbol{\theta}_m$ and $\boldsymbol{\varphi}_{j_m}$ is the j-th undamped mode shape. They are obtained by solving the undamped eigenvalue problem

$$\left(\mathbf{K}-\omega_{j_m}^2\mathbf{M}\right)\boldsymbol{\varphi}_{j_m}=\mathbf{0}$$

and they diagonalize the stiffness and the mass matrices as follows, $\boldsymbol{\Psi}^\intercal\mathbf{K}\boldsymbol{\Psi}=\operatorname{diag}\left(k_{j_1},...,k_{j_m}\right)$ and $\boldsymbol{\Psi}^\intercal\mathbf{M}\boldsymbol{\Psi}=\operatorname{diag}\left(m_{j_1},...,m_{j_m}\right)$, where k_{j_m} and m_{j_m} are referred to as the j-th generalized stiffness and mass of the undamped structure. By introducing these expressions into Equation (7), it finally yields

$$\mathrm{D}_m=\lambda_m\left(k_{j_m}+\lambda_m^2 m_{j_m}\right)^{-1}$$

for the normalization coefficients while the critical damping ratio is given by

$$\xi_{j_m}=\frac{c_{j_m}}{2\sqrt{k_{j_m}m_{j_m}}}$$

where c_{j_m} is the diagonal element of the generalized damping matrix, $\boldsymbol{\Psi}^\intercal\mathbf{C}\boldsymbol{\Psi}$.

2. *The damping ratios are much smaller than one, $\xi_{j_m}\ll 1$ and $\xi_{j_n}\ll 1$.*

Equation (25) therefore becomes

$$\Sigma_{r,mn}=\frac{\pi}{4k_{j_m}k_{j_n}}\frac{\omega_{j_m}\omega_{j_n}}{\left(\xi_{j_m}\omega_{j_m}+\xi_{j_n}\omega_{j_n}\right)+\mathrm{i}\left(\omega_{j_n}-\omega_{j_m}\right)}\left[S_{p,mn}\left(\omega_{j_m}\right)+S_{p,mn}\left(\omega_{j_n}\right)\right]$$

after being truncated at leading order in ξ_{j_m} and ξ_{j_n}.

3. *The damping ratios are the same in both modes, $\xi_{j_m}=\xi_{j_n}=\xi$.*

The covariance hence reads

$$\Sigma_{r,mn}=\frac{\pi}{4k_{j_m}k_{j_n}}\left(\frac{\xi-\mathrm{i}\zeta}{\xi^2+\zeta^2}\right)\left(\frac{\omega_{j_m}\omega_{j_n}}{\omega_{j_m}+\omega_{j_n}}\right)\left[S_{p,mn}\left(\omega_{j_m}\right)+S_{p,mn}\left(\omega_{j_n}\right)\right]$$

where the parameter

$$\zeta=\frac{\omega_{j_n}-\omega_{j_m}}{\omega_{j_n}+\omega_{j_m}}$$

as defined in [12] is introduced.

4. *The natural frequencies are close to each other, $\omega_{j_n}=\omega_{j_m}\left(1+2\zeta\right)$ with $\zeta\ll 1$.*

The covariance is finally expressed by

$$\Sigma_{r,mn}=\frac{\pi}{4k_{j_m}k_{j_n}}\left(\frac{\xi-\mathrm{i}\zeta}{\xi^2+\zeta^2}\right)\left(\frac{\omega_{j_m}+\omega_{j_n}}{2}\right)\left(\frac{S_{p,mn}\left(\omega_{j_m}\right)+S_{p,mn}\left(\omega_{j_n}\right)}{2}\right)$$

as in [12].

5. *The indices m and n are equal to each other.*

At last, the resonant component of the variance

$$\Sigma_{r,mm}=\frac{\pi\omega_{j_m}}{4\xi k_{j_m}^2}S_{p,mn}\left(\omega_{j_m}\right)$$

is also well recovered [7].

Appendix D: Correlation Coefficients of the Modal State Responses

Based on the simple formulas established for the modal state covariances in Section 4, it is possible to write the correlation coefficients of the modal state responses as the sum of a resonant and a loading component as well. Using the same derivation as in [9], it reads

$$\rho_{\hat{q},mn} = \gamma_r \rho_{r,mn} + \gamma_\ell \rho_{\ell,mn}$$

where

$$\gamma_r = \frac{1}{\sqrt{1+r_m^{-1}}\sqrt{1+r_n^{-1}}} \text{ and } \gamma_\ell = \frac{1}{\sqrt{1+r_m}\sqrt{1+r_n}}$$

can be seen as weighting factors. They are related to the resonant-to-loading ratios of the corresponding modal variances as follows

$$r_m = \frac{\Sigma_{r,mm}}{\Sigma_{\ell,mm}} \text{ and } r_n = \frac{\Sigma_{r,nn}}{\Sigma_{\ell,nn}}$$

and accordingly tend towards unity or zero if the modal responses are predominantly driven by their resonant component or their loading component, e.g. $\gamma_r = 1$ and $\gamma_\ell = 0$ if both $r_m \gg 1$ and $r_n \gg 1$, meaning that the responses are fully resonant.

Substituting the appropriate components of the modal variances and covariances that are coming from Equation (25) and Equation (35) in the following expression

$$\rho_{(.),mn} = \frac{\Sigma_{(.),mn}}{\sqrt{\Sigma_{(.),mm}\Sigma_{(.),nn}}}$$

yields the resonant and the loading correlation coefficients. The former is interestingly given by

$$\rho_{r,mn} = i\frac{\sqrt{\upsilon_m \upsilon_n}}{\lambda_m - \lambda_n^*}\left[\Gamma_{mn}\left(\psi_m\right)S_{mn} + \Gamma_{mn}\left(\psi_n\right)S_{nm}\right]$$

which increases if the natural frequencies are getting close to each another and if the values of the coherence function

$$\Gamma_{mn}\left(\omega\right) = \frac{S_{p,mn}\left(\omega\right)}{\sqrt{S_{p,mm}\left(\omega\right)S_{p,nn}\left(\omega\right)}}$$

at $\omega = \psi_m$ and $\omega = \psi_n$ grow as well, together with the spectral ratios

$$S_{mn} = \sqrt{\frac{S_{p,nn}\left(\psi_m\right)}{S_{p,nn}\left(\psi_n\right)}} \text{ and } S_{nm} = \sqrt{\frac{S_{p,mm}\left(\psi_n\right)}{S_{p,mm}\left(\psi_m\right)}}$$

they respectively multiply. The coefficient $\rho_{\ell,mn}$ is not so easily interpretable unless the loading component is quasi-static in both modes, in which case it corresponds to the correlation coefficient of the modal state forces at leading order, i.e. $\rho_{\ell,mn} = \rho_{p,mn}$ if $\alpha_m \ll 1$ and $\alpha_n \ll 1$.